

# The non-uniformity of galaxy cluster metallicity profiles

L. Lovisari<sup>1</sup>★ and T. H. Reiprich<sup>2</sup>

<sup>1</sup>Harvard-Smithsonian Center for Astrophysics, 60 Garden Street, Cambridge, MA 02138, USA

<sup>2</sup>Argelander Institute for Astronomy (AIfA), University of Bonn, Auf dem Hügel 71, D-53121 Bonn, Germany

Accepted 2018 November 13. Received 2018 October 23; in original form 2018 July 20

## ABSTRACT

We study a sample of 207 nearby galaxy groups and clusters observed with *XMM-Newton*. Key aspects of this sample include the large size, the high data quality, and the large diversity of cluster dynamical states. We determine the overall metallicity within  $0.3 R_{500}$  and the radial distribution of the metals. On average, we find a mild dependence of the core metallicity with the average temperature of the system in agreement with previous results. However, we identify the cause of this mild dependence to be due to relaxed systems only; disturbed systems do not show this trend, on average. The large scatter observed in this relation is strongly associated with the dynamical state of the systems: relaxed systems have, on average, a higher metallicity in the core than disturbed objects. The radial profiles of relaxed systems are centrally peaked and show a steep decrease with radius, flattening beyond  $0.3\text{--}0.4 R_{500}$ . The metallicity of disturbed systems is also higher in the centre but at much lower values than what is observed for relaxed objects. This finding is consistent with the picture that cluster mergers mix the abundance distribution by inducing large-scale motions. The scatter of the radial profiles is quite large, but while for relaxed systems it decreases almost monotonically as function of the radius, for disturbed systems it shows a significant boost at large radii. Systems with a central radio source have a flatter profile indicating that central AGNs are an efficient mechanism to uplift and redistribute the metals in the ICM.

**Key words:** galaxies: clusters: intracluster medium – galaxies: groups: general – X-rays: galaxies: clusters.

## 1 INTRODUCTION

Groups and clusters of galaxies are unique environments for elemental abundance measurements because, in view of their deep potential, they are thought to retain all the metals that have been produced over cosmic time. The distribution of the metals in the intracluster medium (ICM) depends on the star formation history (and so the number of supernovae exploded so far) and on the efficiency of the different processes that injected the enriched material into the ICM (Schindler & Diaferio 2008, and references therein). Thus, the study of the abundance and distribution of heavy elements in the ICM provides vital information on the mechanisms responsible for the metal transfer from galaxies to the hot gas, and on the different roles played by mergers, galactic winds, ram-pressure stripping, and AGN outbursts (e.g. Renzini 1997; Rasmussen & Ponman 2009; Fabjan et al. 2010; Höller et al. 2014; Biffi, Mernier & Medvedev 2018). X-ray spectra provide an accurate measurement of the metallicity of the ICM. Since the first X-ray observations of the iron line feature in the 1970s by Mitchell & Culhane (1977), observations

have confirmed that the ICM contains both primordial elements as well as heavy elements (e.g. De Grandi et al. 2004; De Grandi & Molendi 2009). However, metals are not distributed uniformly in the ICM as shown by the studies of the metallicity spatial distribution (e.g. Lovisari et al. 2009; Simionescu et al. 2009; Lovisari, Schindler & Kapferer 2011).

For many years, it was almost impossible to perform metallicity measurements on large fractions of  $R_{500}$ , but with *XMM-Newton*, *Chandra*, and *Suzaku*,<sup>1</sup> it has been possible to derive metallicity profiles for a sizable sample of galaxy groups and clusters (e.g. see the review by Mernier et al. 2018a). These azimuthally averaged profiles show a centrally peaked metallicity distribution in cool-core systems and a relatively flat distribution in non-cool core clusters (e.g. De Grandi et al. 2004; Pratt et al. 2007; Leccardi & Molendi 2008). Outside the cluster core, and irrespective of their central properties, the profiles gently decline out to  $\sim 0.3 R_{500}$ . Beyond that radius, the metallicity is consistent with being flat, as shown by the measurements of the ICM metallicity up to the virial radius for several clusters (e.g. Fujita et al. 2008; Werner et al. 2013;

\* E-mail: [lorenzo.lovisari@cfa.harvard.edu](mailto:lorenzo.lovisari@cfa.harvard.edu)

<sup>1</sup> Because of the malfunction experienced by *Suzaku* in early June 2015, the mission has ended.

Simionescu et al. 2015; Thölken et al. 2016; Ezer et al. 2017; Urban et al. 2017).

A proper modelling of the temperature is crucial; otherwise, the combination of different temperatures, either due to a strong gradient or to a multiphase plasma, can lead to important biases. Buote (2000) showed that fitting a multi-temperature plasma with a single temperature model leads to an underestimation of the metallicity. This effect is known as ‘iron bias’. Rasia et al. (2008) by analysing mock *XMM-Newton* observations of simulated galaxy clusters, showed that projection effects, low spatial resolution, and a particular temperature range (i.e. 2–3 keV) can also lead to a systematic overestimate of the metallicity, known as ‘inverse iron bias’ (see also Simionescu et al. 2009 and Gastaldello et al. 2010).

The effect of these two biases can be an explanation for the trend found by Baumgartner et al. (2005) in the abundance–temperature plot. Using the ASCA archive observations of 273 galaxy clusters, they found a constant abundance at a value of 0.3 solar for high-temperature clusters, an averaged high metallicity (larger by up to a factor of 3 than hotter systems) for the objects in the 2–4 keV energy range, and finally an abundance drop for low-temperature systems. Alternatively, this trend could indicate that different enrichment mechanisms play different roles in clusters with different masses, or that the star formation is more efficient in smaller clusters, as suggested also by optical and near-infrared observations of nearby systems (Lin, Mohr & Stanford 2003; Gonzalez, Zaritsky & Zabludoff 2007). However, it is hard to conceive a mechanism at work only in clusters with a temperature in the 2–4 keV range. It is easier to focus on some possible measurement bias, which has to bias iron abundances high.

A step forward in our understanding of the radial distribution of the abundances in giant elliptical galaxies, groups, and clusters of galaxies was done by the CHEERS (CHEMical Enrichment RGS Sample, see de Plaa et al. 2017) collaboration. Analyzing the 44 CHEERS systems, Mernier et al. (2017) found a significant negative radial metallicity gradient out to  $0.9 R_{500}$  for hot systems ( $kT > 1.7$  keV) and  $0.6 R_{500}$  for cool systems ( $kT < 1.7$  keV) with the latter having, on average, a lower metallicity than the most massive clusters. By construction, the CHEERS sample of 44 objects contains basically only cool-core systems and is dominated by galaxy groups (i.e. average  $kT \lesssim 3$  keV), so it is not representative of the whole cluster population. Other recent studies (Ettori et al. 2015; McDonald et al. 2016; Mantz et al. 2017), although more focused on the evolution of the metallicity with redshift, found a trend of higher metallicity in the innermost regions of cool-core clusters with respect to non-cool-core systems. Moreover, the metallicity in the core was found to be much higher than the metallicity in the outskirts for both relaxed and disturbed systems (e.g. Ettori et al. 2015; Mantz et al. 2017). While these studies are based on more representative galaxy clusters samples for most of the systems, they could not derive very fine spatial binning because of the high cluster redshifts which lead to an average low number of counts per cluster.

In this paper, we investigate the metallicity for a large sample of nearby clusters for which we can derive fine spatial binning and extend the study of the radial metallicity profiles to a larger sample of hot clusters with respect to what has been done with the CHEERS sample. Since a systematic comparison between relaxed and disturbed systems can help to shed light into the mixing of the metals in the ICM, we investigate the impact of the dynamical state in the metallicity profiles of galaxy groups and clusters. Moreover, we investigate the impact of the central AGNs in the distribution of the central abundances.

Throughout the paper, we assume an  $\Lambda$ CDM cosmology with  $H_0 = 70 \text{ km s}^{-1} \text{ Mpc}^{-1}$ ,  $\Omega_\Lambda = 0.7$ , and  $\Omega_m = 0.3$ . The estimated metallicities are all relative to the solar values given by Asplund et al. (2009). The outline of the paper is as follows. The data preparation and analysis is presented in Section 2 and the results in Section 3. In Sections 4 and 5, we discuss the results and present our conclusions.

## 2 OBSERVATIONS AND DATA PREPARATION

### 2.1 Sample selection

The aim of this work is the study of the metal enrichment of the ICM in groups and clusters of galaxies, and the determination of the impact of merging and interactions in the distribution of the metallicity in the ICM. We choose to look at a sample of local galaxy groups and clusters with available *XMM-Newton* data. As input catalogue, we have used the MCXC catalogue (see Piffaretti et al. 2011) and restricted the search to all the objects in the NORAS, REFLEX, and eBCS sub-catalogues (Ebeling et al. 1998, 2000; Böhringer et al. 2000, 2004). By arbitrary use of an upper redshift cut of 0.1, we found 207 objects with useful (i.e. not flared) *XMM-Newton* observations (the list of objects can be found in the Appendix of this paper). Clusters with multiple X-ray peaks, and clusters with an estimated  $0.3 R_{500}^2$  extending beyond the *XMM-Newton* field-of-view (FOV) were removed from the sample.

### 2.2 Data reduction

Observation data files (ODFs) were downloaded from the *XMM-Newton* archive and processed with the XMMSAS v16.0.0 software for data reduction. The initial data processing to generate calibrated event files from raw data was done by running the tasks *emchain* and *epchain*. We only considered single, double, triple, and quadruple events for MOS (i.e.  $\text{PATTERN} \leq 12$ ) and single for pn (i.e.  $\text{PATTERN} = 0$ ) and we applied the standard procedures for bright pixels and hot columns removal (i.e.  $\text{FLAG} = 0$ ) and pn out-of-time correction. All the data sets were cleaned for periods of high background due to the soft protons following the two-stage filtering process procedure extensively described in Lovisari et al. (2011). Briefly, a light curve was first extracted in 100 s bins in the 10–12 (12–14) keV energy band for MOS (pn). A Poisson distribution was fitted to the histogram of this light curve, and  $\pm 2\sigma$  thresholds calculated. The Good Time Interval (GTI) files were produced using these thresholds, and the event lists were filtered accordingly. The new event lists were then re-filtered in a second pass as a safety check for possible flares with soft spectra (e.g. De Luca & Molendi 2004; Nevalainen, Markevitch & Lumb 2005; Pradas & Kerp 2005). In this case, light curves were made with 10s bins in the full [0.3–10] keV band. The point-like sources were detected with the *edetect-chain* task and excluded from the event files. The background event files were cleaned by applying the same PATTERN selection, flare rejection, and point-source removal as for the corresponding target observations.

### 2.3 Background treatment

The total background consists of many different components, each one characterized by distinct temporal, spectral, and spatial varia-

<sup>2</sup>As reference for  $R_{500}$  we used the values provided by Piffaretti et al. (2011)

tions (see the Table<sup>3</sup> summarizing the different components at the *XMM-Newton* background analysis webpage). The main components are the non-vignetted quiescent particle background (QPB) and the cosmic X-ray background (CXB). The CXB can be then subdivided into three subcomponents: thermal emission from the Local Hot Bubble (LHB) and from the Galactic Halo (GH), and an extragalactic component representing the unresolved emission from AGNs.

Since it is the result of the emission of astrophysical sources, the CXB is folded with the response files. To model this component, we followed the method presented in Snowden et al. (2008). Basically, the *XMM-Newton* spectra were fitted simultaneously with the ROSAT All-Sky Survey (RASS) spectra extracted from the region just beyond the virial radius using the available tool<sup>4</sup> at the HEASARC webpage. Both the LHB and GH were described by a thermal emission with temperatures free to vary, and with metallicity and redshift frozen to 1 and 0, respectively. The GH component is absorbed by a gas with total (i.e. neutral and molecular, see Appendix A of this manuscript and Willingale et al. 2013 for more details) hydrogen column density estimated using an online tool,<sup>5</sup> while the LHB is not. The emission to account for the unresolved point sources was modelled with an absorbed power-law with its slope set to 1.41 (De Luca & Molendi 2004).

The QPB consists of a continuum component and several fluorescent lines (see e.g. Mernier et al. 2015 for a list of those lines) which vary across the detector. The filter wheel closed (FWC) observations can be used to estimate the intensity of the various components. We first renormalized the FWC observations following the procedure explained in Zhang et al. (2009). Then, for every interesting region (e.g. the different annuli of the radial profiles), we extracted a spectrum from the same detector area and we fitted it with a broken power law<sup>6</sup> plus 8 (9) Gaussian lines for MOS (pn). We then included such a model in the fit with the normalizations of the broken power law free to vary within a  $\pm 3$  per cent to account for the uncertainties associated with the normalization factor used to rescale the FWC observations which are of the order of 3–5 per cent for relatively short observations.

Finally, we added an extra power law, folded only with the RMF,<sup>7</sup> to the background modelling to account for a residual soft proton contamination which is affecting many observations even after filtering soft flare events. Following the suggestion of the ESAS coobook<sup>8</sup>, we allowed the spectral index of this component free to vary in the range 0.1–1.4. Since this component may be different for MOS and pn detectors, both the slope and normalization are left free to vary in the three detectors and in all the regions of interest (this account, in first approximation, for the proton vignetting).

<sup>3</sup><https://www.cosmos.esa.int/web/xmm-newton/epic-background-components>

<sup>4</sup><http://heasarc.gsfc.nasa.gov/cgi-bin/Tools/xraybg/xraybg.pl>

<sup>5</sup><http://www.swift.ac.uk/analysis/nhtot/index.php>

<sup>6</sup>The first power-law component account for the QPB continuum while the second for a strong low-energy tail due to the intrinsic noise of the detectors.

<sup>7</sup>Ideally, since the protons are funneled toward the detectors by the X-ray mirrors, the power-law should be folded also through the ARF. However, the proton vignetting is different from the photon vignetting (e.g. Marelli et al. 2017) and to date, there is not proton vignetting model available.

<sup>8</sup><ftp://xmm.esac.esa.int/pub/xmm-esas/xmm-esas.pdf>

## 2.4 Spectral analyses

Our goal is to determine both an overall cluster core abundance and, when the data quality allow, the abundance profiles. The objects in our sample span a large range of masses and redshifts, so that their extension in the sky is very different. To have a fair comparison between the core abundances in different systems, we extract spectra from a region within  $0.3 R_{500}$ . This choice allows us to have a high  $S/N = S/\sqrt{S+N}$  and to focus on the radial region where groups and clusters show a metallicity enhancement.

All the regions used for the abundance profiles were centred on the peak of the X-ray emission. The size of the annuli have been determined by requiring a minimum width of  $30''$  and a fixed  $S/N$ . The first requirement ensures that most of the flux (i.e.  $> 80$  per cent, see Zhang et al. 2009) comes from the selected region (due to the *XMM-Newton* point spread function (PSF), some photons scatter from one annulus to another), the second that the abundances are determined with a relatively low and homogeneous uncertainty. Due to the fading of the emission lines for increasing temperatures, hotter systems require a higher  $S/N$  to determine the abundances with a similar uncertainty of galaxy groups. Thus, the  $S/N$  in the 0.3–10 keV band used for different clusters was based on their overall core temperature (i.e.  $< 0.3 R_{500}$ ). The background level for the calculation of the  $S/N$  was determined using the FWC observations for the particle background component and using the results from Lumb et al. (2002) for the foreground component and rescaled to the area of interest. In Appendix B, we give more details about our choice.

All the extracted spectra were re-binned to ensure at least 25 counts per bin which is necessary for the validity of the  $\chi^2$  minimization method.<sup>9</sup> Some clusters are very bright and our requirement of a minimum width for selecting the spectral regions leads to a large number of counts in some spectra (in particular, in the central regions). In that case, a statistical grouping can dramatically oversample the instrument resolution and cause problems during the spectral fitting, so using the SAS task *specgroup* we set the minimum energy width of each group to be at least 1/3 of the full width half-maximum (FWHM) resolution at the central photon energy of the group.

The spectral analysis was done using XSPEC (Arnaud 1996). Spectra were fit in the full (i.e. 0.3–10 keV) energy band with two absorbed (using the total  $N_H$ ) APEC thermal plasma model (Smith et al. 2001) linking the abundances of the two gas phases, as the current instruments do not allow to measure the abundances separately and accurately. In each annulus, the MOS and pn spectra were fitted simultaneously, with linked temperatures and abundances, and all normalizations free to vary to account for the calibration offsets between the different detectors (e.g. Madsen et al. 2017). Beyond  $\sim 2$  arcmin the second temperature component is basically unconstrained, even in presence of relatively good data. Thus, the outer annuli have been fitted with a single APEC model.

## 2.5 Morphology

One goal is to compare the distribution of the metals between relaxed and disturbed systems. Lovisari et al. (2017) found that centroid-

<sup>9</sup>Because of the units (i.e. rates instead of counts) of the RASS spectrum (extracted with the HEASARC background tool v2.5.1) which is jointly fitted with our *XMM-Newton* spectra we cannot use the cstat statistic in XSPEC which requires an integer number of counts per bin. We show in Appendix C that this is not biasing our results.



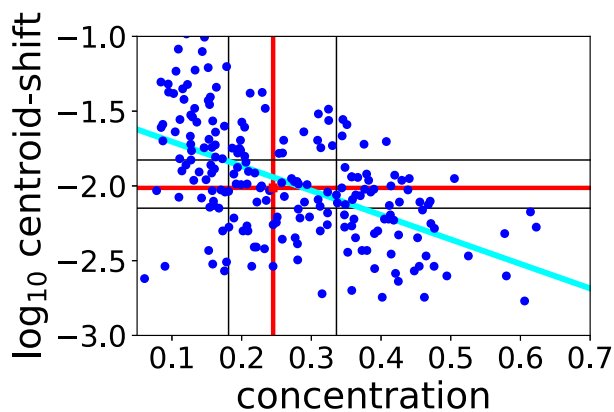


**Figure 1.** Concentration–centroid shift diagram. The red lines indicate the median values while the black lines indicate the 33 and 67percentile. The cyan line represents the best-fit relation to the data points. For the centroid-shift values, we plotted the decimal logarithm.

shift (Mohr, Fabricant & Geller 1993) and concentration (e.g. Santos et al. 2008) are efficient parameters to classify the X-ray cluster morphology. For each cluster, we computed these two parameters within  $0.5 R_{500}$ . We did not consider larger radii because most of the nearby objects lack *XMM–Newton* coverage in the outer regions. The result of the morphological analysis is shown in Fig. 1. By fitting<sup>10</sup> the individual points with a single power law, we get a slope of  $-1.64 \pm 0.18$  with an intrinsic scatter of  $0.33 \pm 0.11$ . Thus, as expected, there is a clear anticorrelation between the two parameters, as also indicated by the Spearman rank coefficient  $r = -0.54$  ( $p < 0.01$ ). The most relaxed objects are the one in the bottom-right quadrant while the most disturbed are in the top-left quadrant. Systems in the top-right panel have a concentrated surface brightness with substantial substructures at larger radii or strong ellipticity and can be considered as objects undergoing a minor merger that did not destroy the core but creates an inhomogeneous distribution of the ICM. Systems in the bottom-left panel can be interpreted as post-merger clusters where enough time to erase most of the inhomogeneities has passed, but not sufficient to rebuild the peaked core.

### 3 RESULTS

#### 3.1 Core metallicities

In Fig. 2, we present the average metallicity,  $A_{\text{core}}$ , determined within  $0.3 R_{500}$  as a function of the cluster temperature as determined within the same radius ( $kT_{\text{core}}$ ). A linear fit to the data gives a mild slope of  $-0.016 \pm 0.005$  (scatter =  $0.121 \pm 0.040$ ) indicating on average lower metallicity in the cores of the most massive systems. This result is confirmed by the median values (shown as green crosses) computed for different temperature intervals, and by the Spearman rank test which returned a value for the temperature–abundance correlation of  $r = -0.18$  ( $p < 0.01$ ). While there are a few groups with very high central metallicity, the mild correlation is confirmed even when excluding systems with  $kT < 1$  keV (slope =  $-0.015 \pm 0.005$ ,  $r = -0.17$  and  $p = 0.02$ ) or with  $kT < 2$  keV (slope =  $-0.016 \pm 0.005$ ,  $r = -0.23$  and  $p < 0.01$ ). Also, there is a clear increasing scatter in the low-mass regime, but we note that our

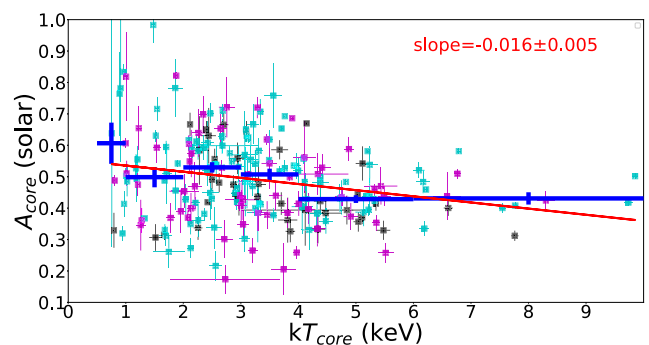


**Figure 2.** Metallicity versus temperature plot obtained fitting the spectra extracted within  $0.3 R_{500}$ . The square points represent the single objects, while the blue crosses are the median values in each temperature bin with the error bars in the Y-axis representing the standard errors. Clusters with and without a central radio source are shown in cyan and magenta, respectively. In black, we show the clusters which are not covered by the NVSS catalogue. The solid red line represents the best fit to all the unbinned data.

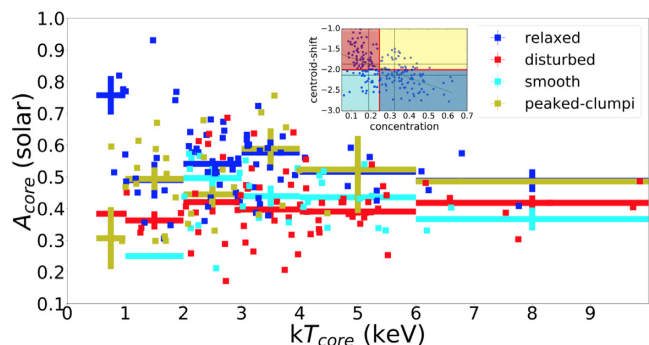


**Figure 3.** The same as in Fig. 2 but highlighting with different colours clusters in the different quadrants of the concentration–centroid shift diagram. We used the medians of concentration and centroid-shift distributions to split the sample.

sample has a relatively low number of very massive clusters since these are intrinsically rare systems.

Relaxed and disturbed clusters may not be sharing the same average abundance in the studied volume. If so, their different fractions in different samples have an impact in the result shown in Fig. 2 and may lead to a wrong interpretation. Using the concentration and centroid-shift medians, we subdivided the sample in relaxed clusters (i.e. high concentration and low centroid-shift, bottom-right quadrant in Fig. 1) and disturbed (i.e. low concentration and high centroid-shift, top-left quadrant in Fig. 1) clusters. We also show clusters that are classified as relaxed using the concentration and disturbed with the centroid-shift (top-right quadrant) and relaxed using the centroid-shift and disturbed by the concentration (bottom-left quadrant). The results are shown in Fig. 3. Apart from the innermost bin, the metallicities of the peaked-clumpi clusters are consistent with the ones of the relaxed systems and the metallicities of the smooth clusters are very similar with the ones of the disturbed systems. While this may be an indication that the driver for the high metallicity is the presence of a cool-core, we note that the metallicity distribution that we obtain by splitting the sample using only the concentration is very similar to the one we obtain by splitting the sample using only the centroid-shift.

Keeping in mind that there is no strong boundary between relaxed and disturbed systems and that the morphological parameters

<sup>10</sup>Throughout the paper the fits were performed using the Bayesian code by Kelly (2007).

have some scatter due to projection effects, the result shows a very clear trend: the relaxed clusters have, on average, a higher metallicity in the core than the disturbed systems at all temperatures. Moreover, by fitting relaxed and disturbed systems independently, the abundance–temperature correlation disappears for dynamically active clusters. The Spearman rank test gives a probability  $p = 0.95$  of no correlation for the disturbed systems. Relaxed clusters still show the mild relation (slope =  $-0.022 \pm 0.010$ ,  $r = -0.19$  and  $p = 0.11$ ) but it becomes more uncertain when excluding  $kT < 1$  keV (slope =  $-0.014 \pm 0.011$ ,  $r = -0.09$  and  $p = 0.48$ ) or  $kT < 2$  keV (slope =  $-0.016 \pm 0.008$ ,  $r = -0.20$  and  $p = 0.15$ ) systems.

### 3.2 Abundance profiles

The projected temperature and metallicity profiles are plotted in Fig. 4, scaled by  $R_{500}$ . The temperature profiles (*top-left-hand panel*), renormalized by the average temperature estimated within  $0.3 R_{500}$ , behave quite universally increasing from the centre and reaching the maximum at  $0.1\text{--}0.2 R_{500}$  and a slow decline beyond that peak. The metallicity profiles, show a large scatter in the centre with values ranging between  $0.3$  and  $2 Z_{\odot}$ , but show also a universal decrease with radius with a flattening beyond  $\sim 0.4 R_{500}$ . In Fig. 5, we show the stacked profiles that have been estimated using Monte Carlo simulations. We performed 10,000 realizations of the profiles by randomly varying the observational data points of the temperature and metallicity profiles to determine new distributions. The randomization was derived from the distribution of measurement values and errors. The randomization of the data points with the radius, scaled by  $R_{500}$ , was done using a truncated Gaussian distribution to bound the points to the extraction area. For each realization and each radial bin, we computed the average metallicity and the scatter to obtain a distribution of values. The median values of 10 000 realizations are shown in Fig. 5 with the 68 per cent uncertainties taken from the distributions. In Appendix D, we compare the stacked profile derived here with the one derived using the weighted mean. The stacked metallicity profile (*right-hand panel* of Fig. 5) is compared with what was found by Leccardi & Molendi (2008) who analysed a sample of massive systems (i.e.  $kT > 3$  keV) and by Mernier et al. (2017) who analysed a sample of cool-core systems mostly in the low-mass regime. Our average profiles are in quite good agreement with the results of Leccardi & Molendi (2008). The slightly higher metallicity obtained in their work can be easily explained by the use of a different  $N_H$  (Leccardi & Molendi 2008 used the LAB values instead of the total  $N_H$  used in this work). A higher  $N_H$  (as assumed in this work) returns, in general, a smaller metallicity value, mainly due to the change in the measured temperature. For average column densities ( $3\text{--}5 \times 10^{20} \text{ cm}^{-2}$ ), the impact can be of the order of 5–10 per cent, enough to compensate for the observed difference. See Appendix A for more details.

If we exclude the inner and outermost data points, our metallicities are systematically lower (5–15 per cent) than the ones by Mernier et al. (2017). This deviation does not arise from a different column density because the total  $N_H$  values were also used by Mernier et al. (2017) when fitting the data. Indeed, their sample by construction includes only relaxed, cool-core systems while our sample includes also very disturbed systems. To understand if these disturbed systems can justify the observed difference, we split the sample based on their dynamical state. To emphasize the difference, we only consider relaxed (i.e. the ones in the bottom-right quadrant of Fig. 1) and disturbed (i.e. the ones in the top-left quadrant) clusters. The result is shown in Fig. 6 and summarized in Table 1. Indeed, the relaxed systems showed a strong drop from the centre

to  $\sim 0.2\text{--}0.3 R_{500}$  where the profiles flatten. On the contrary, disturbed systems show a much shallower drop. However, even when comparing only the relaxed systems, there is still some tension between our results and the average profiles obtained by Mernier et al. (2017) beyond the central bin. Thus, the difference cannot entirely be explained by the presence of a larger fraction of disturbed systems in our sample. Differences may also arise from the use of different spectral fitting packages and plasma codes (e.g. Mernier et al. 2017 performed their analysis using the SPEX package, see Kaastra, Mewe & Nieuwenhuijzen 1996, and an updated version of the MEKAL code, see Mewe, Gronenschild & van den Oord 1985). So, a more detailed investigation is required to understand the cause of this difference but it is beyond the scope of this paper.

The scatter decreases almost monotonically from the centre to the outer regions for relaxed systems while for disturbed clusters it reaches a minimum at  $\sim 0.2\text{--}0.3 R_{500}$  and then it increases again in the outer regions (where anyway we have only a few measurements). The scatter in the cores is much larger for relaxed systems while disturbed systems show a larger scatter beyond  $\sim 0.2 R_{500}$ . The increase of the scatter in the outer regions can be seen in Fig. 7 where we showed the metallicity profiles normalized by  $A_{\text{core}}$ . Relaxed clusters (blue points) behave very similarly, with the highest value in the centre and a drop of already a factor of 2 at  $\sim 0.1 R_{500}$  for most of the systems. Beyond  $\sim 0.4 R_{500}$ , the metallicity of relaxed systems is a factor of 4–5 smaller than in the centre. For disturbed systems instead, it is not always a monotonic decrease of the metallicity. The drop from the centre is not uniform from cluster to cluster with the different profiles showing a very inhomogeneous distribution with the effect to significantly increase the scatter in the outer regions. In some cases, the outer metallicity values are higher than the values measured in the centre. This is the case for  $\sim 30$  per cent of the clusters in the top-left quadrant (disturbed) and for a few in the top-right (peaked-clumpi) or bottom-left (smooth) quadrants. The only cluster that was classified as relaxed and shows an increasing metallicity in the outer regions is A2142, a massive cluster that shows a significant dynamical activity at large scales as shown by, e.g. Owers, Nulsen & Couch (2011), Rossetti et al. (2013), and Tchernin et al. (2016).

### 3.3 AGN feedback

AGNs have been shown to be an efficient mechanism for uplifting the metals from the central regions to the outskirts of a few individual galaxy clusters (e.g. Simionescu et al. 2009; Doria et al. 2012; Kirkpatrick & McNamara 2015). Using hydrodynamical simulations, Biffi et al. (2017) showed that AGNs are indeed expected to distribute the metal-rich gas out to large radii. Here, with a large sample of galaxy clusters, we statistically investigate the impact of AGN feedback on the metallicity profiles subdividing our sample in clusters with and without a central radio source (CRS). The presence of the CRS was identified using the NVSS catalogue by requiring a maximum separation of 50 kpc from the X-ray peak as suggested by Mittal et al. (2009) (see also Edwards et al. 2007). Both distribution of clusters with and without a CRS cover a large range of temperatures (see Fig. 2). For the comparison of the metallicity profiles, we only used the relaxed systems of our sample. This ensures that any effect is not related to the different profiles of relaxed and disturbed systems shown in the previous section. We also verified that even for this subsample, both galaxy clusters with and without a CRS span a broad temperature range ensuring that any effect is independent of the weak dependence of the metallicity with the temperature discussed in Section 3.1. The results are shown

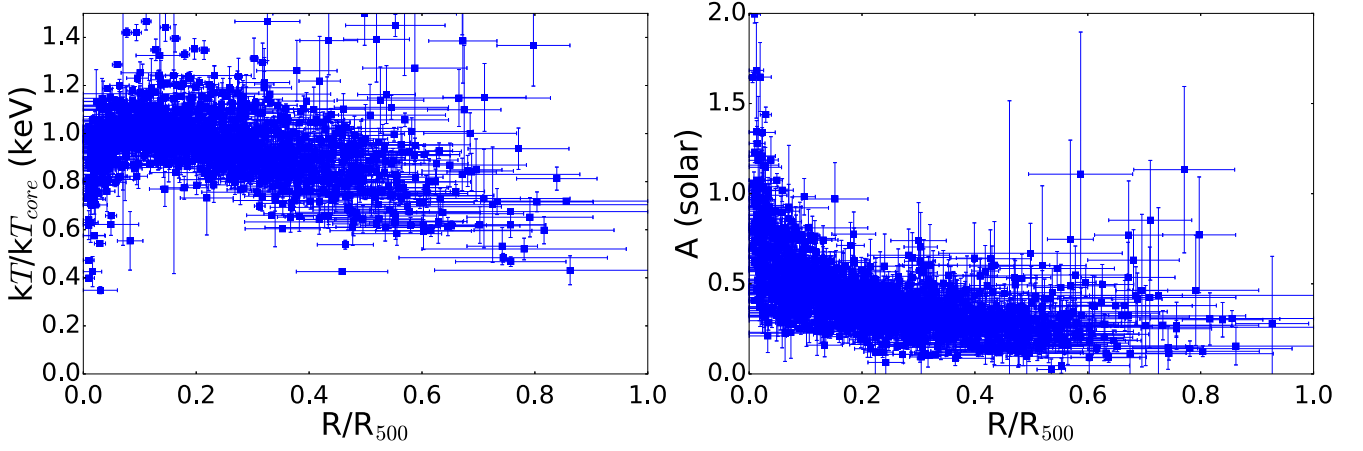


**Figure 4.** Temperature (*left*) and abundance (*right*) profiles scaled by  $R_{500}$ . The temperature profiles have been also normalized by the average temperature measured within  $0.3 R_{500}$ .

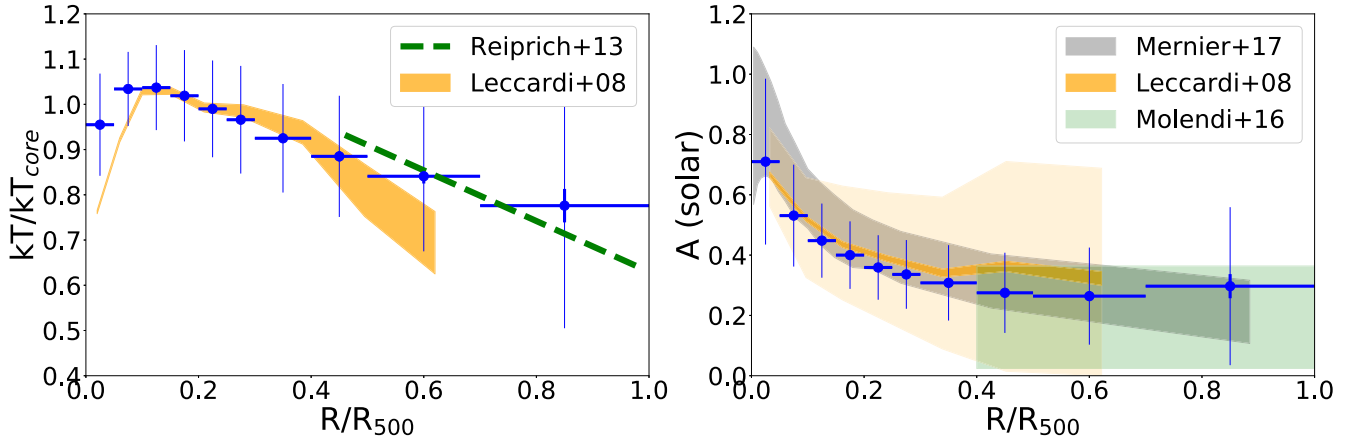


**Figure 5.** Median temperature (*left*) and abundance (*right*) profiles scaled by  $R_{500}$ . The temperature profiles have been also normalized by the average temperature measured within  $0.3 R_{500}$ . Data points and errorbars show the median values and the scatter of the measurements in each radial bin. The statistical errors are shown as a thicker errorbar (smaller than the symbol size for most data points). The grey shadow area represents the average profile, including the scatter, derived by Mernier et al. 2017. The orange area represents the average profiles obtained by Leccardi & Molendi 2008 with the dark and light colours illustrating the statistical uncertainties and the scatter, respectively. The green dotted line in the left-hand panel is the best linear fit derived by Reiprich et al. 2013 in the galaxy clusters outskirts. The green area in the right-hand panel shows the best estimate of the metallicity beyond  $0.4 R_{500}$  derived by Molendi et al. 2016.

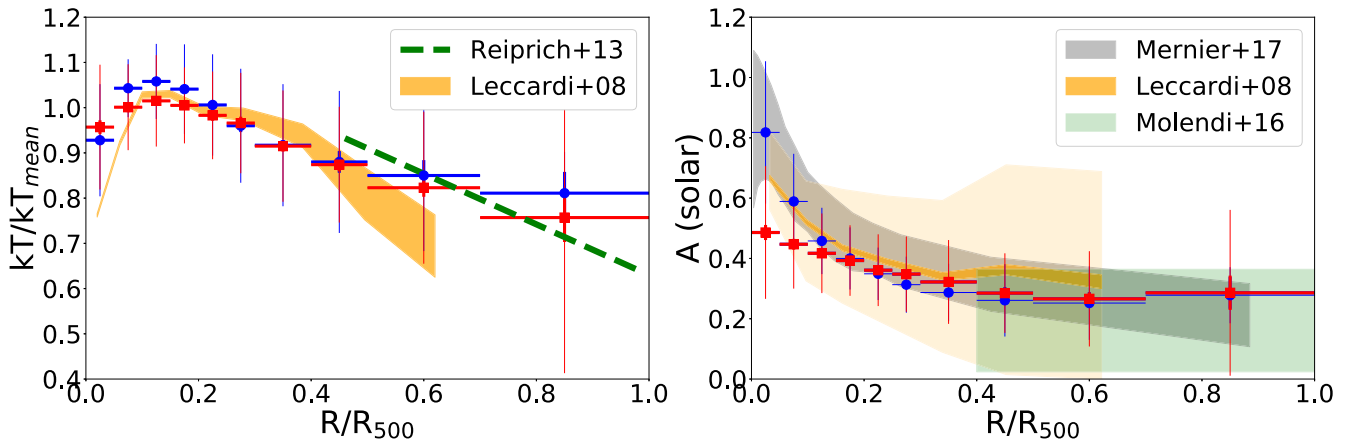


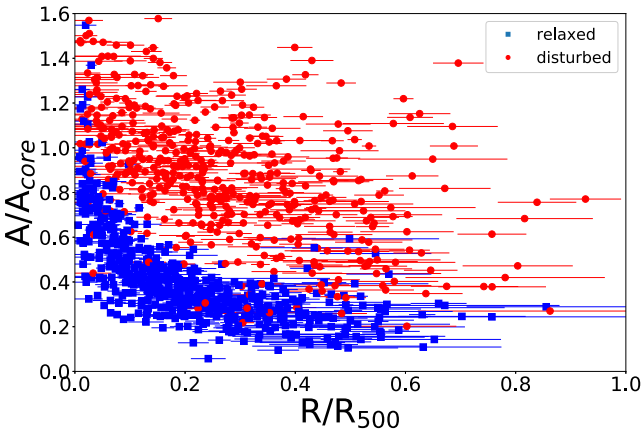
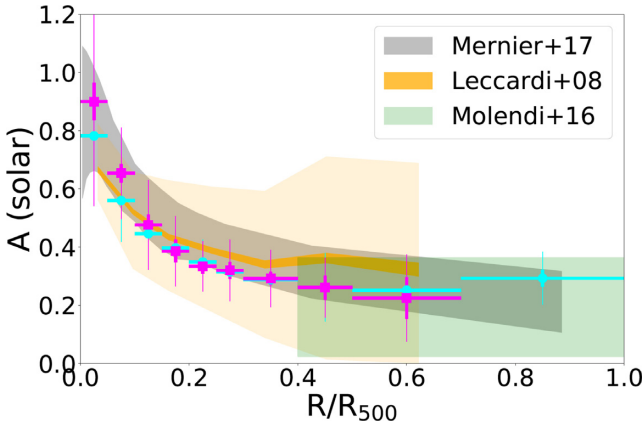
**Figure 6.** Stacked temperature (*left*) and metallicity (*right*) profiles for relaxed (blue points) and disturbed (red squares) systems, using the median value of the concentration parameter to classify the systems.

**Table 1.** Average metallicity profiles for relaxed and disturbed galaxy groups and clusters.

Radius ( $r/r_{500}$ )	Relaxed		Disturbed	
	A (Solar)	Scatter	A (solar)	Scatter
0.00–0.05	$0.818 \pm 0.015$	$0.236 \pm 0.009$	$0.486 \pm 0.025$	$0.220 \pm 0.011$
0.05–0.10	$0.589 \pm 0.014$	$0.158 \pm 0.006$	$0.447 \pm 0.018$	$0.147 \pm 0.015$
0.10–0.15	$0.458 \pm 0.011$	$0.110 \pm 0.006$	$0.417 \pm 0.014$	$0.132 \pm 0.009$
0.15–0.20	$0.400 \pm 0.011$	$0.103 \pm 0.005$	$0.393 \pm 0.014$	$0.117 \pm 0.006$
0.20–0.25	$0.349 \pm 0.011$	$0.087 \pm 0.005$	$0.361 \pm 0.016$	$0.119 \pm 0.005$
0.25–0.30	$0.313 \pm 0.011$	$0.093 \pm 0.006$	$0.348 \pm 0.017$	$0.125 \pm 0.006$
0.30–0.40	$0.287 \pm 0.010$	$0.095 \pm 0.005$	$0.322 \pm 0.014$	$0.139 \pm 0.006$
0.40–0.50	$0.261 \pm 0.020$	$0.120 \pm 0.007$	$0.285 \pm 0.017$	$0.132 \pm 0.007$
0.50–0.70	$0.252 \pm 0.022$	$0.122 \pm 0.010$	$0.266 \pm 0.021$	$0.158 \pm 0.007$
0.70–1.00	$0.278 \pm 0.053$	$0.093 \pm 0.023$	$0.286 \pm 0.057$	$0.275 \pm 0.035$

**Table 2.** Average metallicity profiles for galaxy groups and clusters with or without a central radio source.

Radius ( $r/r_{500}$ )	RS		no RS	
	A (Solar)	Scatter	A (Solar)	Scatter
0.00–0.05	$0.782 \pm 0.015$	$0.215 \pm 0.010$	$0.900 \pm 0.064$	$0.359 \pm 0.018$
0.05–0.10	$0.560 \pm 0.012$	$0.141 \pm 0.008$	$0.654 \pm 0.032$	$0.157 \pm 0.023$
0.10–0.15	$0.446 \pm 0.010$	$0.093 \pm 0.005$	$0.476 \pm 0.036$	$0.154 \pm 0.017$
0.15–0.20	$0.397 \pm 0.011$	$0.089 \pm 0.005$	$0.386 \pm 0.039$	$0.120 \pm 0.013$
0.20–0.25	$0.349 \pm 0.012$	$0.076 \pm 0.004$	$0.334 \pm 0.026$	$0.086 \pm 0.008$
0.25–0.30	$0.315 \pm 0.012$	$0.083 \pm 0.006$	$0.320 \pm 0.029$	$0.106 \pm 0.009$
0.30–0.40	$0.288 \pm 0.010$	$0.087 \pm 0.004$	$0.292 \pm 0.023$	$0.098 \pm 0.009$
0.40–0.50	$0.262 \pm 0.022$	$0.118 \pm 0.007$	$0.261 \pm 0.041$	$0.103 \pm 0.017$
0.50–0.70	$0.252 \pm 0.025$	$0.118 \pm 0.009$	$0.225 \pm 0.071$	$0.150 \pm 0.059$
0.70–1.00	$0.293 \pm 0.029$	$0.091 \pm 0.025$	–	–

**Figure 7.** Metallicity profiles normalized by  $A_{\text{core}}$ . Relaxed systems are shown in blue while disturbed clusters are shown in red. Errorbars in the Y-axis are not shown.**Figure 8.** Stacked average metallicity profiles for galaxy groups and clusters with (cyan points) or without (magenta points) a central radio source. We used only the relaxed systems (i.e. the bottom-right-hand panel of Fig. 1).

in Fig. 8 and summarized in Table 2. The profiles of the systems hosting a CRS are much flatter, i.e. in the centre, the metallicity is systematically lower, at 10–20 per cent level (although the scatter is also large), than the ones without a CRS. The effect is expected to be much stronger at the groups scale because AGNs are expected to leave stronger imprints at the galaxy group scale due to their shall-

lower potential. Unfortunately, although there is a hint for a steeper profiles for the groups without a central radio source we only have five systems and that question should be confirmed with a larger sample.

### 3.4 Shaping the abundance profile in the cores

The shape of the metallicity profiles depends on the individual cluster histories. However, if we use the concentration–centroid shift diagram as a proxy of the state of relaxation of a cluster, we can study how the central abundance and shape of the profiles change as the dynamical state varies.

Despite the large scatter, morphological parameters are a measure of how relaxed the cluster is. Thus, for example, the higher is the concentration the more relaxed is expected to be the cluster and the more time is probably passed since the last major merger. As a consequence, the expected abundance in the core of these clusters is expected to be higher because it hasn't been mixed and redistributed by large-scale motions induced through the merger. In Fig. 9 (*top panel*) we show the positive correlation (slope =  $0.39 \pm 0.06$ , scatter =  $0.109 \pm 0.04$ ) between the abundance and the concentration. The moderate correlation is confirmed also by the Spearman rank test ( $r = 0.47$ ,  $p < 0.01$ ). The most peaked clusters have, on average, a higher metallicity in the centre. The tendency of having the highest metallicity in the most relaxed systems is also confirmed by the negative correlation between the abundance and the centroid–shift (*middle panel*).

While some clusters are clearly relaxed (e.g. high concentration and low centroid–shift) or disturbed (low concentration and high centroid–shift), there are some clusters that are not so easily defined. As discussed in Section 2.5, they can be interpreted as clusters evolving in one or another dynamical state (i.e. relaxed objects which show infalling substructures, or post-merger objects that are slowly moving back to the relaxed status). In the bottom panel of Fig. 9, we compare the metallicity profiles of the most relaxed (clusters with a concentration above the 67 percentile and a centroid–shift below the 33 percentile) and most disturbed objects (clusters with a concentration below the 33 percentile and a centroid–shift above the 67 percentile) with the peaky-clumpi and smooth systems. Since there are a few low temperature systems with very high metallicity (see Fig. 2) to make the plot, we excluded all the systems with  $kT < 2$  keV to make sure that any observed trend is not associated with them. Apart from the most relaxed systems which show a hint of lower metallicity, beyond  $\sim 0.3 R_{500}$  all the profiles are basically flat and behave very similarly. However, in the



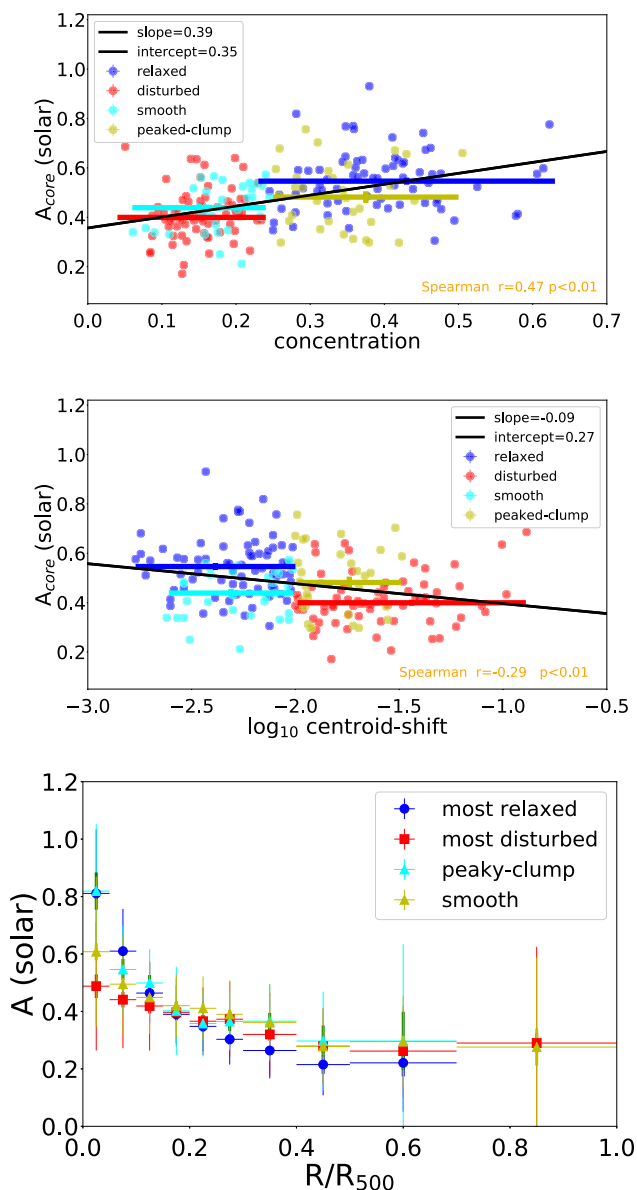


**Figure 9.** *Top:* abundance–concentration plot. The data points are the individual measurements and the colours are the same as in Fig. 3 with the bold lines representing the median of the distribution for each subsample. The core abundances have been derived within  $0.3 R_{500}$  and the concentration within  $0.5 R_{500}$ . The cyan line is the best fit to the individual data points. The measurement errors for both the concentration and the core abundance are not shown for visualization purposes but they are accounted for in the fit. *Middle:* the same as in the top-panel but for the centroid–shift. *Bottom:* stacked metallicity profiles for groups and clusters populating a different region of the concentration–centroid shift diagram as shown in the inset plot. The most relaxed clusters are the ones with a concentration above the 67 percentile and a centroid–shift lower than the 33 percentile. The most disturbed clusters are the ones with a concentration below the 33 percentile and a centroid–shift higher than the 67 percentile. Peaky-clumpi and smooth clusters are as defined in Section 2.5.

core, they look quite different, with the metallicity profiles steepening and moving from the most disturbed to the most relaxed. This behaviour is confirmed also when cutting at higher temperatures. Moreover, we note that while relaxed and peaky clusters share a similar core abundance they have a different metallicity profile. In

the innermost bin, the metallicity is very similar (both still have a core) but the most relaxed systems have a much steeper profile.

## 4 DISCUSSION

### 4.1 Whole core abundances

Our analysis of the global abundances is based on the inner regions of galaxy groups and clusters. We find that this choice emphasizes the differences between systems with different properties (e.g. temperature, dynamical state). In fact, the largest difference in the metallicity profiles arises in the innermost regions while in the outskirts the divergence is not significant (in part, because the quality of the data and the limitation of the current instruments do not allow to measure eventual small metal variation). By fitting the data points of the individual measurements, we obtained the weak dependence of the metallicity with cluster mass in agreement with what found by previous studies (e.g. see Balestra et al. 2007; Yates, Thomas & Henriques 2017). The higher metallicity in low-mass systems together with their lower gas mass with respect to hot clusters (e.g. Lovisari, Reiprich & Schellenberger 2015) was interpreted as an indication for a lower star formation efficiency in massive systems (e.g. Zhang et al. 2011). However, this metal dependence disappears when only the disturbed systems are considered. There is still a mild dependence for relaxed systems but it is possibly dominated by a very few low-temperature objects with extremely high metallicity. In fact, when removing low- $kT$  systems, the dependence is much more uncertain. This agrees well with the result by Mernier et al. (2018b) who found a very similar average Fe enrichment within  $0.1 R_{500}$  for a sample of 44 relaxed elliptical galaxies, groups, and clusters. Thus, a different fraction of relaxed and disturbed clusters at different temperatures in the analyzed samples might lead to a different observed dependence. Anyhow, we note that while there are 32 groups and clusters with a global metallicity within  $0.3 R_{500}$  higher than 0.6 solar for temperatures below 4 keV, there is only one cluster (out of 13 relaxed systems) with such a high abundance at high temperatures. One possible explanation is that it is very difficult to build a very massive galaxy cluster without undergoing a major merger (or multiple minor mergers). During these events the core is disrupted or strongly affected, with the final effect of lowering the central metallicity.  $N$ -body simulations find that small clusters and groups have a lower merger rate (e.g. Neistein & Dekel 2008, Genel et al. 2009), so that their central metallicity patterns are not destroyed during their evolution, and they can potentially reach high values. Another possible explanation is that in massive galaxy clusters the contribution to the enrichment from galaxies is probably negligible because galaxies comprise less than 5 per cent of the baryons in rich clusters. At the groups scale instead, the baryon fraction in galaxy members is at least equal to that of the hot gas (Giodini et al. 2009), so enriched material from galaxies can significantly impact the amount of metals present in the ICM. That would explain the slightly higher metallicity observed in the centre of the low-mass systems. However, low-mass systems also show in some cases a quite low metallicity ( $Z \leq 0.3 Z_{\odot}$ ) which is not observed at high temperatures. While there are possible systematic uncertainties related to multitemperature structure, this might indicate that indeed different processes are at work in different systems and that for some reason the star-formation efficiency in some groups is not efficient. These low-metallicity clusters are almost equally split in clusters with and without a CRS so the presence/absence of central AGN is probably not the cause of the high scatter observed in the low-mass regime.



## 4.2 Average profiles

Fig. 4 shows the individual projected temperature (*left-hand panel*) and metallicity (*right-hand panel*) profiles as a function of the radius rescaled by  $R_{500}$ . It can clearly be seen that the dispersion is much larger in the core where some individual systems show a strongly peaked metallicity while others show lower values. This large scatter is independent of their dynamical state. The metallicity then declines with radius and seems pretty constant (within the large scatter) beyond  $0.3\text{--}0.4 R_{500}$ . Fig. 5 shows the average profiles, split by their dynamical state. While the metallicity profiles of relaxed and disturbed systems differ in the central regions ( $R < 0.1 R_{500}$ ), at large radii (i.e. beyond  $0.4 R_{500}$ ) they are consistent with a flat distribution: a fit with a constant for  $R > R_{500}$  gives a value of  $0.28 \pm 0.11 Z_{\odot}$  (but see Molendi et al. 2016 for a description of the challenges in determining the metallicity in the outskirts). In the  $0.3\text{--}0.4 R_{500}$  region, the average profile of disturbed systems shows hints of a metallicity excess with respect to the average profile of relaxed clusters. This effect was also obtained with hydrodynamical simulations by Biffi et al. (2017). It is possibly due to the metals that have been spread out from the centre during the merging. The difference of the core metallicity as function of the cluster dynamical state, and the convergence of the profiles for relaxed and disturbed systems at large radii was also observed by Mantz et al. (2017).

The difference between the profiles of relaxed and disturbed systems was already observed by De Grandi & Molendi (2001) who analysed a sample of 17 hot systems with ASCA data. Their results showed a much larger metallicity gradient for cool-core systems than non-cool-core clusters. The moderate gradient observed for disturbed systems was interpreted as the remnant of a much stronger gradient that has not been completely erased by the merger events. Our results support this scenario as shown in the bottom panel of Fig. 9. The most relaxed objects share the same metallicity in the centre of the peaky-clumpi objects in agreement with the fact that the cores of both subsamples are unaffected. However, the metallicity profile for the most relaxed clusters is much steeper than the one of the peaky-clumpi clusters for which the disturbance detected with the morphological parameters is probably associated with a large-scale mixing. The most disturbed objects (in red) show a very weak gradient of the metallicity in the centre, while the smooth systems (in green) show hint of a metallicity increase toward the centre. Thus, there is a strict connection between the observed metallicity profiles and the morphological properties of the systems. Major mergers are able to erase the metallicity pattern in the centre but also minor mergers have an impact on the metallicity profiles. However, even in presence of a major merger, we might still be seeing a moderate metallicity peak in the centre if we are in the very early merger stage where the metals have not been mixed yet, or in an old merger stage where a new abundance gradient is forming again.

## 4.3 AGNs feedback

The feedback from the central supermassive black holes has an impact on the distribution of the hot ICM, so they can potentially affect the shape of the metallicity profiles. AGNs manifest as central radio sources, which jets are often responsible for disturbances of the ICM. One example are the so-called X-ray cavities associated with inflating lobes of radio-emitting plasma. Some of the work done by these cavities is used to lift the metal-enriched gas (e.g. Kirkpatrick & McNamara 2015) implying that AGNs may be able to mix the metals on scales of several hundreds of kpc. In Fig. 8, we compared the metallicity profile for relaxed systems hosting a

central AGN with the one without a central AGN and we found that indeed the former has a much flatter profile. This is interpreted as the redistribution of the enriched gas due to the AGNs. Another hint to support this hypothesis is the different impact of the AGNs on the profiles of galaxy groups and galaxy clusters, with the latter less affected by the presence of the CRS in the centre. The effects of feedback from central AGNs is, in fact, expected to be more important at the scale of groups because of their shallower potential wells. It would be important to confirm this apparent trend with an even larger sample. We observe hints that profiles of groups and clusters with a central AGN have also a higher metallicity in the  $0.2\text{--}0.4 R_{500}$  region. This is the first observational confirmation, albeit still at low significance, for the prediction of hydrodynamical simulations by Biffi et al. (2017), who found that including the AGN feedback in the hydrodynamical simulations strongly reduces the central metallicity and increases the metallicity in the outer regions.

## 4.4 Low- and high-mass systems

Mernier et al. (2016, 2017) reported a much lower metallicity outside the core in galaxy groups with respect to the one in galaxy clusters while in the core they found a similar abundance. The median temperature of their sample was 1.7 keV and it is the value they used to characterize groups and clusters. Since we excluded all the nearby systems for which the *XMM-Newton* FOV is not large enough to measure at least  $0.3 R_{500}$ , our sample does not include most of the galaxy groups analyzed by Mernier et al. (2016, 2017). Moreover, by construction, we did not analyse bright and nearby elliptical galaxies, so the number of systems in our sample with an average temperature lower than 1.7 keV is limited to only 18 galaxy groups. A more reasonable value for our sample is a cut at 3 keV, so that the groups and cluster subsamples have roughly a similar size. Moreover, since in the previous section we found that the presence/absence of a CRS may impact the metallicity profiles, for each subsample (i.e. groups and clusters) we investigate objects with and without a CRS separately. Despite the large scatter, in both cases we found that galaxy groups have a higher metallicity than galaxy clusters within  $\sim 0.1 R_{500}$ . The metallicity in groups drops quite fast and galaxy clusters show a higher metallicity beyond that radius in agreement with the finding by Mernier et al. (2016, 2017). The higher metallicity in the outer regions of galaxy clusters is also confirmed if we only consider the relaxed systems (i.e. bottom-left quadrant in Fig. 1) to avoid any bias from the metallicity–dynamical state connection discussed in Section 4.2.

## 5 CONCLUSIONS

We derived the average metallicity within  $0.3 R_{500}$  for 207 groups and clusters in the local Universe ( $z < 0.1$ ) observed with *XMM-Newton*. For 156 systems, the data were sufficient also to determine the averaged azimuthal metallicity profiles up to a minimum of  $0.4 R_{500}$  and a maximum of  $\approx R_{500}$ . Our main findings are the following:

- (i) A mild anticorrelation between the average metallicity and temperature within  $0.3 R_{500}$ . However, relaxed systems have typically higher mean metallicity than disturbed objects and when fitting the abundance–temperature correlation for relaxed and disturbed objects independently, this mild anticorrelation weakens/disappears.
- (ii) The metallicity profiles rapidly decrease from the centre to  $0.2\text{--}0.3 R_{500}$  where they flatten and stay constant out to large radii. While behaving very similarly beyond  $0.1\text{--}0.2 R_{500}$ , the profiles

for relaxed and disturbed systems diverge in the centre where the former have a much more peaked distribution.

(iii) The average profile determined for relaxed systems hosting a CRS is flatter than the one determined for relaxed systems without a CRS. We interpret this in the sense that central AGNs can modify the shape of the metallicity profiles. Supportive of this interpretation is that the difference between the profiles with and without CRS is more accentuated at the galaxy groups scale where AGNs feedback is thought to be stronger due to their lower potential wells.

(iv) Using the concentration–centroid shift diagram to classify different stages of the clusters’ dynamical state, we found that the more relaxed the clusters are, the more the metallicity profiles become steeper in the cores. We argued that this depends on how much time has passed since the last major merger: shortly after the merging, the metallicity pattern is completely erased but if nothing new happens, then the metallicity profile slowly begins to rebuild.

(v) Galaxy groups and clusters with similar properties (e.g. with or without CRS) have a different metallicity profile suggesting that the mechanisms at work to enrich and mix the hot gas may not be the same at all mass scales.

(vi) We showed that any trend depends on the applied sample selection and that, consequently, the sample needs to be well-characterized (in terms of mass, morphological state, central AGN) to enable meaningful interpretations.

## ACKNOWLEDGEMENTS

We thank the anonymous referee for the useful report which helped to improve the quality of the paper. We acknowledge Gerrit Schellenberger for the help and fruitful discussion. LL and THR acknowledge support from the German Research Association (DFG) through the Transregional Collaborative Research Centre TRR33 ‘The Dark Universe’ (project B18) and support from the German Aerospace Agency (DLR) with funds from the Ministry of Economy and Technology (BMWi) through grant 50 OR 1514. LL also acknowledges support from NASA through contract NNX17AD83G.

## REFERENCES

- Arnaud K. A., 1996, in Jacoby G. H., Barnes J., eds, *Astronomical Society of the Pacific Conference Series Vol. 101, Astronomical Data Analysis Software and Systems V.*, p. 17
- Asplund M., Grevesse N., Sauval A. J., Scott P., 2009, *ARA&A*, 47, 481
- Balestra I., Tozzi P., Ettori S., Rosati P., Borgani S., Mainieri V., Norman C., Viola M., 2007, *A&A*, 462, 429
- Baumgartner W. H., Loewenstein M., Horner D. J., Mushotzky R. F., 2005, *ApJ*, 620, 680
- Biffi V. et al., 2017, *MNRAS*, 468, 531
- Biffi V., Mernier F., Medvedev P., 2018, *MNRAS*, 481, 2213, preprint ()
- Böhringer H. et al., 2000, *ApJS*, 129, 435
- Böhringer H. et al., 2004, *A&A*, 425, 367
- Buote D. A., 2000, *MNRAS*, 311, 176
- De Grandi S., Molendi S., 2001, *ApJ*, 551, 153
- De Grandi S., Molendi S., 2009, *A&A*, 508, 565
- De Grandi S., Ettori S., Longhetti M., Molendi S., 2004, *A&A*, 419, 7
- De Luca A., Molendi S., 2004, *A&A*, 419, 837
- de Plaa J. et al., 2017, *A&A*, 607, A98
- Doria A., Gitti M., Ettori S., Brighenti F., Nulsen P. E. J., McNamara B. R., 2012, *ApJ*, 753, 47
- Ebeling H., Edge A. C., Böhringer H., Allen S. W., Crawford C. S., Fabian A. C., Voges W., Huchra J. P., 1998, *MNRAS*, 301, 881
- Ebeling H., Edge A. C., Allen S. W., Crawford C. S., Fabian A. C., Huchra J. P., 2000, *MNRAS*, 318, 333
- Edwards L. O. V., Hudson M. J., Balogh M. L., Smith R. J., 2007, *MNRAS*, 379, 100
- Ettori S., Baldi A., Balestra I., Gastaldello F., Molendi S., Tozzi P., 2015, *A&A*, 578, A46
- Ezer C., Bulbul E., Nihal Ercan E., Smith R. K., Bautz M. W., Loewenstein M., McDonald M., Miller E. D., 2017, *ApJ*, 836, 110
- Fabjan D., Borgani S., Tornatore L., Saro A., Murante G., Dolag K., 2010, *MNRAS*, 401, 1670
- Fujita Y., Tawa N., Hayashida K., Takizawa M., Matsumoto H., Okabe N., Reiprich T. H., 2008, *PASJ*, 60, S343
- Gastaldello F. et al., 2010, *A&A*, 522, A34
- Genel S., Genzel R., Bouché N., Naab T., Sternberg A., 2009, *ApJ*, 701, 2002
- Giodini S. et al., 2009, *ApJ*, 703, 982
- Gonzalez A. H., Zaritsky D., Zabludoff A. I., 2007, *ApJ*, 666, 147
- Höller H., Stöckl J., Benson A., Haider M., Steinhauser D., Lovisari L., Pranger F., 2014, *A&A*, 569, A31
- Humphrey P. J., Liu W., Buote D. A., 2009, *ApJ*, 693, 822
- Kaastra J. S., Mewe R., Nieuwenhuijzen H., 1996, in Yamashita K., Watanabe T., eds, *UV and X-ray Spectroscopy of Astrophysical and Laboratory Plasmas*, p. 411
- Kalberla P. M. W., Burton W. B., Hartmann D., Arnal E. M., Bajaja E., Morras R., Pöppel W. G. L., 2005, *A&A*, 440, 775
- Kelly B. C., 2007, *ApJ*, 665, 1489
- Kirkpatrick C. C., McNamara B. R., 2015, *MNRAS*, 452, 4361
- Leccardi A., Molendi S., 2008, *A&A*, 487, 461
- Lin Y.-T., Mohr J. J., Stanford S. A., 2003, *ApJ*, 591, 749
- Lovisari L. et al., 2017, *ApJ*, 846, 51
- Lovisari L., Kapferer W., Schindler S., Ferrari C., 2009, *A&A*, 508, 191
- Lovisari L., Schindler S., Kapferer W., 2011, *A&A*, 528, A60
- Lovisari L., Reiprich T. H., Schellenberger G., 2015, *A&A*, 573, A118
- Lumb D. H., Warwick R. S., Page M., De Luca A., 2002, *A&A*, 389, 93
- Madsen K. K., Beardmore A. P., Forster K., Guainazzi M., Marshall H. L., Miller E. D., Page K. L., Stuhlinger M., 2017, *AJ*, 153, 2
- Mantz A. B., Allen S. W., Morris R. G., Simionescu A., Urban O., Werner N., Zhuravleva I., 2017, *MNRAS*, 472, 2877
- Marelli M. et al., 2017, *Exp. Astron.*, 44, 297
- McDonald M. et al., 2016, *ApJ*, 826, 124
- Mernier F. et al., 2017, *A&A*, 603, A80
- Mernier F. et al., 2018a, preprint ([arXiv:1811.01967](https://arxiv.org/abs/1811.01967))
- Mernier F. et al., 2018b, *MNRAS*, 478, L116()
- Mernier F., de Plaa J., Lovisari L., Pinto C., Zhang Y.-Y., Kaastra J. S., Werner N., Simionescu A., 2015, *A&A*, 575, A37
- Mernier F., de Plaa J., Pinto C., Kaastra J. S., Kosec P., Zhang Y.-Y., Mao J., Werner N., 2016, *A&A*, 592, A157
- Mewe R., Gronenschild E. H. B. M., van den Oord G. H. J., 1985, *A&AS*, 62, 197
- Mitchell R. J., Culhane J. L., 1977, *MNRAS*, 178, 75P
- Mittal R., Hudson D. S., Reiprich T. H., Clarke T., 2009, *A&A*, 501, 835
- Mohr J. J., Fabricant D. G., Geller M. J., 1993, *ApJ*, 413, 492
- Molendi S., Eckert D., De Grandi S., Ettori S., Gastaldello F., Ghizzardi S., Pratt G. W., Rossetti M., 2016, *A&A*, 586, A32
- Neistein E., Dekel A., 2008, *MNRAS*, 388, 1792
- Nevalainen J., Markevitch M., Lumb D., 2005, *ApJ*, 629, 172
- Owers M. S., Nulsen P. E. J., Couch W. J., 2011, *ApJ*, 741, 122
- Piffaretti R., Arnaud M., Pratt G. W., Pointecouteau E., Melin J.-B., 2011, *A&A*, 534, A109
- Pradas J., Kerp J., 2005, *A&A*, 443, 721
- Pratt G. W., Böhringer H., Croston J. H., Arnaud M., Borgani S., Finoguenov A., Temple R. F., 2007, *A&A*, 461, 71
- Rasia E., Mazzotta P., Bourdin H., Borgani S., Tornatore L., Ettori S., Dolag K., Moscardini L., 2008, *ApJ*, 674, 728
- Rasmussen J., Ponman T. J., 2009, *MNRAS*, 399, 239
- Reiprich T. H., Basu K., Ettori S., Israel H., Lovisari L., Molendi S., Pointecouteau E., Roncarelli M., 2013, *Space Sci. Rev.*, 177, 195
- Renzini A., 1997, *ApJ*, 488, 35
- Rossetti M., Eckert D., De Grandi S., Gastaldello F., Ghizzardi S., Roediger E., Molendi S., 2013, *A&A*, 556, A44

- Santos J. S., Rosati P., Tozzi P., Böhringer H., Ettori S., Bignamini A., 2008, *A&A*, 483, 35
- Schellenberger G., Reiprich T. H., Lovisari L., Nevalainen J., David L., 2015, *A&A*, 575, A30
- Schindler S., Diaferio A., 2008, *Space Sci. Rev.*, 134, 363
- Simionescu A., Werner N., Böhringer H., Kaastra J. S., Finoguenov A., Brüggén M., Nulsen P. E. J., 2009, *A&A*, 493, 409
- Simionescu A., Werner N., Urban O., Allen S. W., Ichinohe Y., Zhuravleva I., 2015, *ApJ*, 811, L25
- Smith R. K., Brickhouse N. S., Liedahl D. A., Raymond J. C., 2001, *ApJ*, 556, L91
- Snowden S. L., Mushotzky R. F., Kuntz K. D., Davis D. S., 2008, *A&A*, 478, 615
- Tchernin C. et al., 2016, *A&A*, 595, A42
- Thölken S., Lovisari L., Reiprich T. H., Hasenbusch J., 2016, *A&A*, 592, A37
- Urban O., Werner N., Allen S. W., Simionescu A., Mantz A., 2017, *MNRAS*, 470, 4583
- Werner N., Urban O., Simionescu A., Allen S. W., 2013, *Nature*, 502, 656
- Willingale R., Starling R. L. C., Beardmore A. P., Tanvir N. R., O'Brien P. T., 2013, *MNRAS*, 431, 394
- Yates R. M., Thomas P. A., Henriques B. M. B., 2017, *MNRAS*, 464, 3169
- Zhang Y.-Y., Reiprich T. H., Finoguenov A., Hudson D. S., Sarazin C. L., 2009, *ApJ*, 699, 1178
- Zhang Y.-Y., Laganá T. F., Pierini D., Puchwein E., Schneider P., Reiprich T. H., 2011, *A&A*, 535, A78

## APPENDIX A: IMPACT OF THE USED COLUMN DENSITY ON THE MEASURED ABUNDANCE

X-rays can be absorbed by material along the line of sight. It follows that accurate cluster property measurements requires a careful estimation of the absorption. Commonly, this effect is quoted as the equivalent column density of hydrogen although generally it is due to heavier elements. The abundance of these metals is usually traced by measuring the neutral hydrogen HI column density with 21 cm measurements. A frequently used HI-survey is the Leiden/Argentine/Bonn (LAB) survey (Kalberla et al. 2005). This only provides the neutral hydrogen contribution along the line of sight but does not account for the molecular and ionized hydrogen. A measure of the molecular hydrogen has been provided by Willingale et al. (2013) using the dust extinction  $E(B - V)$  measured in the  $B$  and  $V$  band and calibrated using the X-ray afterglows of Gamma Ray Bursts. As shown by, e.g., Schellenberger et al. (2015) the contribution of the molecular component starts to be significant above  $\sim 5 \times 10^{20} \text{ cm}^{-2}$  and can have a significant impact on the measured temperatures, and therefore, also on the abundances. In Fig. A1 (top panel), we show how the measured metallicity varies by using the LAB or total  $N_H$ . While for low- $N_H$  values (i.e.  $\leq 3 \times 10^{20} \text{ cm}^{-2}$ ), the effect is almost negligible, for higher values (i.e.  $3\text{--}6 \times 10^{20} \text{ cm}^{-2}$ ), it can be as high as 10 per cent. For higher column densities, the impact is even more dramatic and can reach 50 per cent or more.

In Fig. A1 (bottom panel), we compare the column densities obtained by leaving  $N_H$  free to vary during the fit of the spectra extracted within  $R_{500}$ , with  $N_{H, \text{LAB}}$  and  $N_{H, \text{TOT}}$ , respectively. Indeed, the agreement between the fitted values and  $N_{H, \text{TOT}}$  is much better, in particular for large  $N_H$  values. We note that in a few cases, even using  $N_{H, \text{TOT}}$  is not enough and leaves clear residuals in the spectral fit. In these cases, we use the  $N_{H, \text{FREE}}$  to determine the spectral properties used in this paper. At low column densities, the fitted  $N_H$  values are in general lower (in agreement with the finding by Schellenberger et al. 2015) than the tabulated  $N_H$  but the uncertainties in the measurements are pretty large.

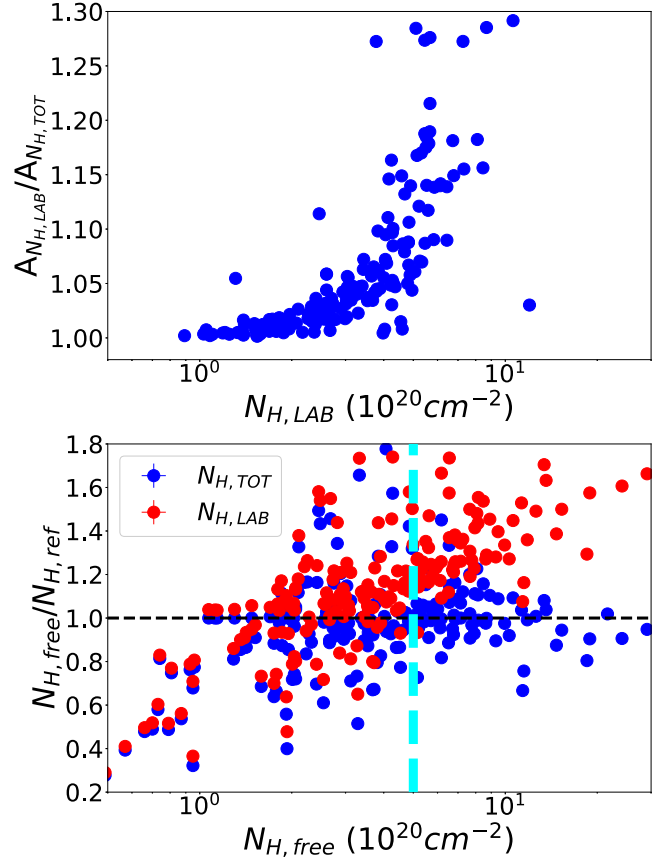


**Figure A1.** *top:* the ratio between the abundance derived using  $N_{H, \text{LAB}}$  and  $N_{H, \text{TOT}}$  as function of the LAB value. (*bottom*) ratio between the measured  $N_H$  value (i.e. left free to vary in the fit) and  $N_{H, \text{LAB}}$  (red points) and  $N_{H, \text{TOT}}$  (blue points), respectively. The agreement between the fitted value and  $N_{H, \text{TOT}}$  is quite good, in particular above  $\sim 5 \times 10^{20} \text{ cm}^{-2}$  (cyan line) when fitting  $N_H$  becomes less challenging.

## APPENDIX B: S/N FOR THE METAL PROFILES

Due to the fading of the emission lines, it is harder to estimate the metallicity of the high temperature galaxy clusters than the one of cooler galaxy groups. To have a fairly similar selection of the annuli for galaxy clusters with different temperatures, we ran a set of simulations to estimate the required  $S/N$  necessary to have an estimate of the metallicity better than  $\sim 30$  per cent.

We assumed an extraction region of 5 arcmin, an exposure time of 30 ks, redshift = 0.05,  $N_H = 3 \times 10^{20} \text{ cm}^{-2}$ , and an input metallicity of 0.3 solar. The model of the particle background components has been determined using the FWC observations while the foreground emission using the results from Lumb et al. (2002) and rescaled to an area of  $5'$  radius. Then, the normalization of the cluster thermal component was modified to match the required  $S/N$ . Each combination was ran 1000 times and for every realization we computed the relative error for the temperature and metallicity. In Fig. B1, we show the median values of the distribution of relative errors with the 68 per cent errors taken from the distributions. For cool systems (e.g.  $kT < 3 \text{ keV}$ ), an  $S/N$  of 50 is sufficient to get metallicity measurements better than 30 per cent. For hotter systems, we had to use a  $S/N$  of 100 or 150.

Note that for most of the clusters in our sample the  $S/N$  in the innermost annuli is still much higher than our requirement because of the minimum bin size of 30 arcsec. We checked our measured val-



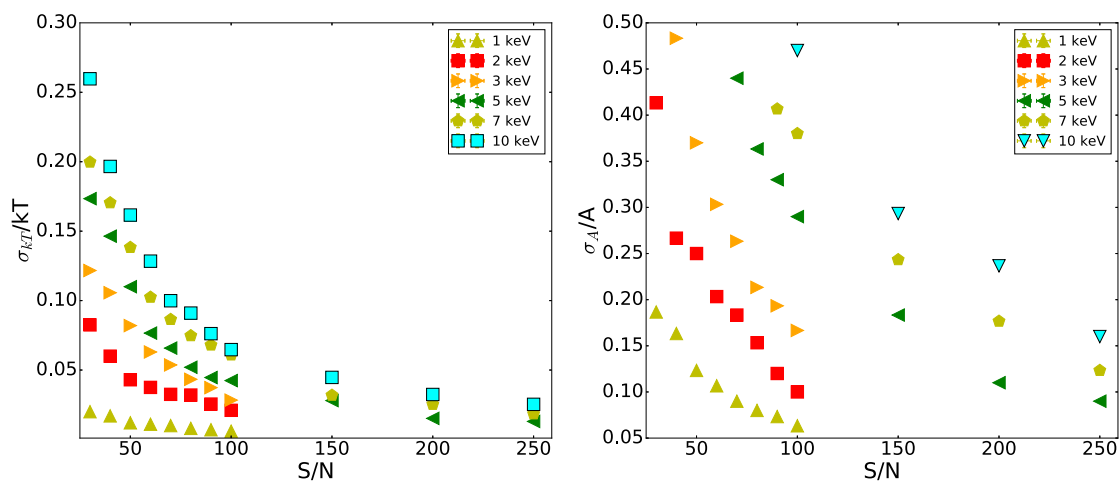


**Figure B1.** *left:* The relative error of the temperature (*left*) and metal (*right*) measurements as a function of the  $S/N$  for clusters with different temperatures. These are just statistical errors. For plotting purposes, we only show the results for five input temperatures.

ues to make sure that the fitted relative errors are consistent with the expectation from our simulations, and indeed the agreement is fairly good although in the outermost bins we usually find slightly larger relative errors. This is possibly due to the stronger fluorescence lines in the outer CCDs compared to the ones determined in the central CCD and that were assumed for our simulations. Anyway, that does not affect in any way the conclusion of the paper.

### APPENDIX C: SPECTRAL FITTING

As explained in Section 2.4, for each cluster we are doing a joint fit of our *XMM-Newton* spectra and the RASS spectrum obtained with the X-ray background tool by HEASARC, for which we cannot use the cstat statistic<sup>11</sup> in XSPEC. Several studies discussed that the use of the  $\chi^2$  statistic may bias the results (e.g. Humphrey, Liu & Buote 2009), although the effect on the metallicity seems smaller than the one on the temperature for a large range of  $S/N$  (e.g. Mantz et al. 2017). To investigate whether our results suffer from a measurement bias, we ran a set of simulations. We simulated spectra using an exposure of 20 ks for  $kT = 1, 3$ , and 5 keV, a metallicity of 0.5, and a redshift of 0.05. The model for the background has been added following the procedure described in Appendix B. Then, the normalization of the cluster component was modified to match the interesting  $S/N$ : for 1 keV plasma we investigated spectra with an  $S/N = 30, 50$ , and 100 while for hotter systems  $S/N = 50, 100$ , and 150. Each combination was ran 1000 times. In Fig. C1, we show the median of the best fit values obtained by fitting the spectra with cstat or  $\chi^2$  statistic. When using  $\chi^2$ , we fitted the spectra with standard binning (i.e. minimum of 25 counts per bin, referred as group in the figure) and spectra binned to get a minimum energy width of each group of at least 1/3 of the full width half maximum (FWHM) resolution at the central photon energy of the group (referred as specgroup in the figure). The second choice strongly decreases the number of bin that will be fitted. We find that biases in the abundance determination in the  $S/N$  regime of interest (see Appendix B for the choice of the  $S/N$ ) using the  $\chi^2$  statistic are in agreement with what obtained using cstat, in particular when the grouping is done by requiring a minimum energy resolution. This is because the bias is expected to

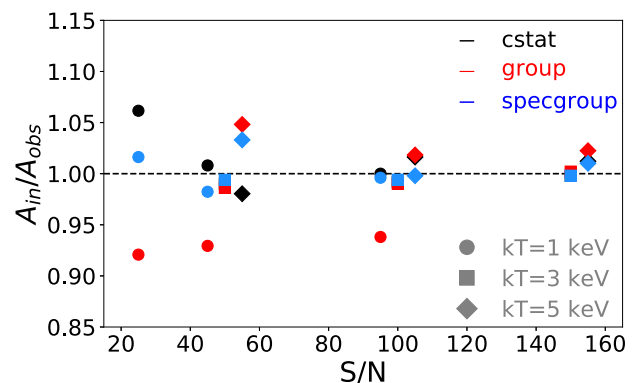


**Figure C1.** The points are the median of the best-fit values of the metallicity divided by the input metallicity obtained for each combination of temperature,  $S/N$ , and fitting method. Each combination was ran 1000 times. The circles refer to  $kT = 1$  keV, the squares to  $kT = 3$  keV, and diamonds to 5 keV plasma. Circles and diamonds have been shifted by  $-5$  and  $+5$  in  $S/N$  for visualization purposes.

increase with the ratio between the square root of the number of counts and the number of bin (i.e.  $\sqrt{N_C}/N_{bin}$ , see Humphrey et al. 2009). While with standard grouping,  $N_{bin}$  always increases with increasing  $N_C$  this is not the case when setting a minimum energy width for the binning. Thus, when the number of counts is high (which is almost always the case in our spectra thanks to the high  $S/N$  required) the  $\sqrt{N_C}/N_{bin}$  ratio becomes larger than 1 and the bias is comparable with what one obtain with cstat.

### APPENDIX D: WEIGHTED MEAN VS MEDIAN METALLICITIES

The binned profiles presented in this paper have been obtained using Monte Carlo simulations instead of the weighted mean as done, e.g., by Mernier et al. (2017) and Leccardi & Molendi (2008). In Fig. D1 (*top panel*), we show the comparison between the stacked profile for the relaxed clusters obtained using MC simulations and the profile that one obtains following the prescription for the weighted mean (red triangles) given in Leccardi & Molendi (2008). The latter appears to be systematically lower at all radii. The reason is that some objects in our sample have a very good data quality leading to very

<sup>11</sup>Note that in a recent release the support for counts statistics and the creation of a counts-based spectrum has been added to the tool.



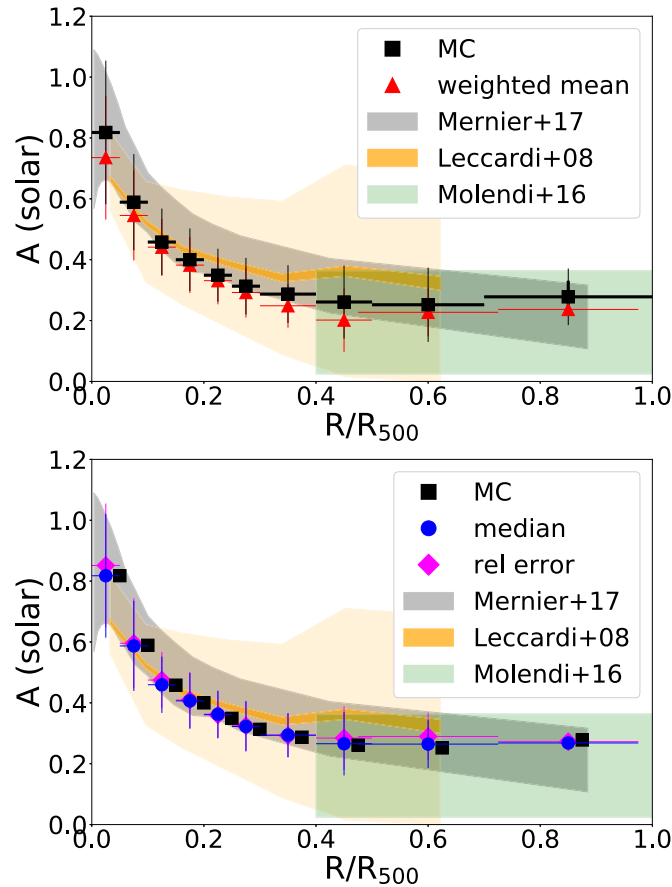


**Figure D1.** *top*: stacked metallicity profiles for the most relaxed (bottom-left quadrant in Fig. 1) galaxy groups and clusters derived using the weighted mean (red triangles) and compared with the stacked profile derived with the MC simulations (black points). (*bottom*) the same as in the left-hand panel but comparing the profile obtained using the median (blue points) of the distribution with the weighted mean profile obtained using the relative errors as weights (magenta diamonds) and compared with the stacked profile derived with the MC simulations (black points, slightly shifted and without errorbars for visualization purposes).

small statistical uncertainties (in particular in the centre where we set a minimum width of 30 arcsec per annulus) of their measured metallicities. As a consequence, these galaxy groups and clusters have an important contribution in the final average metallicity profile. These long observations are often associated with particular classes of clusters, like strong cool cores or major mergers in contrast to the less exciting weak cool core clusters. Moreover, the quality of the data also depends on the fraction of flares and so the clean exposure time, introducing a bias, on top of the archival bias, that cannot be easily quantified. When removing six clusters (i.e. A4038, Hydra-A, A0085, AS1101, 2A0335, and A2199) that contribute to  $\sim 65$  per cent of the total weight in the innermost annuli, this trend disappears and the two profiles overlap with only a residual  $\sim 5$  per cent difference in the innermost bin. Those clusters are among the ones with the longest observations, and so delivering smallest statistical errors and so significantly contributing to the weighted mean values. Moreover, even with similar data quality clusters with lower metallicities have a smaller statistical errors and so biasing toward smaller values the average profile. To avoid this problem one can use either the median values of each radial bin or

use the relative errors instead of the statistical errors as weights. In Fig. D1 (*bottom panel*) we compare the profile obtained using the MC simulations with the profile obtained using the median values (blue points) with the weighted mean profile using the relative errors as weight (magenta diamonds). The agreement is good even without removing any cluster from the sample because the weight of every individual system is much smaller than in the case of the weight based on the inverse of the square of the individual errors.

## APPENDIX E: CLUSTER PROPERTIES

In Table E1 we provide the list of clusters (column 1) used in this paper. Coordinates and redshifts are shown in columns 2–4. In columns 5–6 we provide the list of XMM-Newton observations which we investigated and the corresponding clean exposure times for MOS1, MOS2, and pn. The masses used to estimate  $R_{500}$  are given in column 7 and are taken from Piffaretti et al. (2011). In columns 8–10, we provided the estimated core abundances, concentration, and centroid-shift parameters.

Table E1. Properties of the clusters.

Name	RA	DEC	redshift	ObsID	$t_{\text{exp}}$ [ks]	$M_{500}$ [ $10^{14} M_{\odot}$ ]	$A_{\text{core}}$ [solar]	$w$	$c$
NGC4936	13 04 16.7	−30 30 55	0.012	0204540101	11.7, 12.9, 6.5	0.225	$0.332 \pm 0.031$	$0.014 \pm 0.001$	$0.156 \pm 0.002$
A3565	13 36 38.8	−33 57 30	0.012	0672870101	30.6, 33.7, 19.4	0.128	$0.450 \pm 0.045$	$0.017 \pm 0.001$	$0.194 \pm 0.002$
A1060	10 36 41.8	−27 31 28	0.013	0206230101	31.4, 32.9, 23.9	0.994	$0.471 \pm 0.007$	$0.009 \pm 0.001$	$0.181 \pm 0.000$
NGC1550	04 19 37.8	+ 02 24 50	0.055	0152150101	19.0, 18.9, 14.8	0.703	$0.549 \pm 0.004$	$0.004 \pm 0.000$	$0.352 \pm 0.001$
				0723800401	47.3, 48.5, 29.5				
				0723800501	79.2, 79.5, 59.6				
S0753	14 03 35.9	−33 59 16	0.014	0741930101	108.5, 111.5, 89.7	0.267	$0.209 \pm 0.008$	$0.010 \pm 0.001$	$0.229 \pm 0.001$
HCG62	12 53 05.5	−09 12 01	0.015	0504780501	78.7, 79.5, 58.5	0.272	$0.268 \pm 0.005$	$0.011 \pm 0.001$	$0.441 \pm 0.001$
NGC499	01 23 12.2	+ 33 27 40	0.150	0402360101	20.0, 21.1, 10.6	0.362	$0.429 \pm 0.010$	$0.009 \pm 0.001$	$0.439 \pm 0.002$
S0840	04 58 55.1	−00 29 21	0.015	0673180401	19.0, 21.8, 12.6	0.114	$0.306 \pm 0.052$	$0.019 \pm 0.001$	$0.376 \pm 0.007$
NGC3411	10 50 25.5	−12 50 47	0.015	0146510301	20.1, 20.8, 17.3	0.411	$0.776 \pm 0.021$	$0.005 \pm 0.000$	$0.623 \pm 0.003$
A0262	01 52 46.8	+ 36 09 05	0.017	0109980101	21.3, 21.4, 15.5	1.189	$0.485 \pm 0.007$	$0.005 \pm 0.000$	$0.245 \pm 0.001$
				0504780201	25.9, 28.4, 14.5				
NGC507	01 23 41.0	+ 33 15 40	0.017	0723800301	80.5, 83.2, 60.0	0.611	$0.432 \pm 0.004$	$0.033 \pm 0.002$	$0.325 \pm 0.001$
NGC777	02 00 16.5	+ 31 26 11	0.170	0203610301	5.2, 5.2, 1.6	0.285	$0.819 \pm 0.142$	$0.007 \pm 0.000$	$0.281 \pm 0.003$
				0304160301	4.9, 6.3, 1.6				
AWM7	02 54 29.5	+ 41 34 18	0.017	0135950301	27.4, 27.8, 22.0	1.835	$0.642 \pm 0.003$	$0.017 \pm 0.001$	$0.199 \pm 0.000$
				0605540101	109.2, 112.2, 83.7				
MKW1s	09 20 00.5	+ 01 02 24	0.018	0673180201	14.8, 16.7, 5.3	0.134	$0.595 \pm 0.338$	$0.017 \pm 0.001$	$0.254 \pm 0.005$
NGC0410	01 10 58.1	+ 33 08 58	0.015	0203610201	13.2, 12.9, 10.6	0.215	$0.297 \pm 0.022$	$0.012 \pm 0.001$	$0.420 \pm 0.005$
A0189	01 25 24.7	+ 01 44 28	0.033	0109860101	32.9, 34.3, 27.3	0.370	$0.473 \pm 0.012$	$0.004 \pm 0.000$	$0.380 \pm 0.002$
MKW4	12 04 25.2	+ 01 54 02	0.020	0723800601	15.3, 17.4, 8.4	0.677	$0.768 \pm 0.010$	$0.005 \pm 0.000$	$0.348 \pm 0.001$
				0723800701	54.5, 55.7, 34.4				
HCG97	23 47 24.4	−02 18 52	0.022	0152860101	24.5, 24.0, 20.7	0.245	$0.342 \pm 0.021$	$0.026 \pm 0.001$	$0.351 \pm 0.004$
NGC5171	13 29 27.8	+ 11 43 23	0.023	0041180801	16.1, 15.7, 11.4	0.170	$0.225 \pm 0.034$	$0.026 \pm 0.001$	$0.087 \pm 0.002$
S0301	02 49 36.9	−31 11 19	0.022	0146510401	29.9, 29.4, 23.0	0.447	$0.494 \pm 0.010$	$0.010 \pm 0.001$	$0.414 \pm 0.002$
A3581	14 07 28.1	−27 00 55	0.023	0205990101	33.1, 33.7, 28.2	1.081	$0.457 \pm 0.004$	$0.008 \pm 0.000$	$0.470 \pm 0.001$
				0504780301	41.5, 47.2, 26.3				
NGC1132	02 52 49.4	−01 16 27	0.024	0151490101	19.7, 20.4, 15.0	0.466	$0.047 \pm 0.041$	$0.003 \pm 0.000$	$0.280 \pm 0.003$
A2877	01 10 00.4	−45 55 22	0.025	0204540201	19.2, 19.3, 15.2	0.710	$0.420 \pm 0.027$	$0.039 \pm 0.002$	$0.155 \pm 0.001$
A0400	02 57 38.9	+ 06 00 22	0.024	0404010101	25.6, 26.0, 16.7	0.801	$0.597 \pm 0.021$	$0.037 \pm 0.002$	$0.152 \pm 0.001$
Zw1745	17 36 22.1	+ 68 03 26	0.025	0203610401	20.8, 21.2, 15.7	0.239	$0.261 \pm 0.027$	$0.063 \pm 0.004$	$0.178 \pm 0.004$
IC1867	02 55 51.3	+ 09 18 48	0.026	0203610501	12.1, 11.8, 4.5	0.325	$0.748 \pm 0.110$	$0.005 \pm 0.000$	$0.358 \pm 0.005$
NGC4325	12 23 06.5	+ 10 37 26	0.026	0108860101	17.9, 17.6, 13.2	0.559	$0.570 \pm 0.013$	$0.002 \pm 0.000$	$0.358 \pm 0.005$
MKW8	14 40 38.2	+ 03 28 35	0.026	0300210701	19.7, 20.3, 14.5	0.735	$0.395 \pm 0.023$	$0.021 \pm 0.001$	$0.153 \pm 0.001$
R2315.7−0222	23 15 45.2	−02 22 37	0.025	0501110101	30.8, 30.3, 24.2	0.584	$0.535 \pm 0.018$	$0.019 \pm 0.001$	$0.330 \pm 0.002$
Ophiucus	17 12 24.7	−23 21 01	0.055	0505150101	27.4, 29.0, 14.9	5.312	$0.483 \pm 0.008$	$0.033 \pm 0.002$	$0.133 \pm 0.000$
NGC4104	12 06 37.4	+ 28 11 01	0.028	0301900401	11.1, 11.1, 8.4	0.418	$0.269 \pm 0.021$	$0.006 \pm 0.000$	$0.250 \pm 0.004$
A2199	16 28 38.0	+ 39 32 55	0.030	0723801101	46.2, 47.7, 36.3	2.963	$0.506 \pm 0.003$	$0.008 \pm 0.001$	$0.310 \pm 0.000$
				0723801201	47.1, 47.6, 39.5				
A4038	23 47 43.2	−28 08 29	0.028	0204460101	26.6, 25.7, 22.8	2.038	$0.436 \pm 0.005$	$0.006 \pm 0.000$	$0.405 \pm 0.001$
				0723800801	44.0, 44.1, 36.3				
R0953.2−1558	09 53 12.1	−15 58 52	0.030	0140210201	34.2, 34.8, 28.1	0.418	$0.400 \pm 0.015$	$0.009 \pm 0.001$	$0.385 \pm 0.003$
IC1262	17 33 02.6	+ 43 45 46	0.031	0741580201	5.9, 6.0, 3.2	0.859	$0.312 \pm 0.018$	$0.011 \pm 0.001$	$0.358 \pm 0.004$
A2634	23 38 25.7	+ 27 00 45	0.031	0002960101	7.1, 7.4, 3.8	1.215	$0.339 \pm 0.038$	$0.002 \pm 0.000$	$0.061 \pm 0.001$
				0505210801	6.8, 8.9, 2.7				
III Zw54	03 41 16.9	+ 15 24 27	0.031	0505230401	35.2, 38.4, 23.4	1.130	$0.263 \pm 0.011$	$0.004 \pm 0.000$	$0.277 \pm 0.001$
A0496	04 33 38.4	−13 15 33	0.033	0506260301	51.1, 53.0, 36.3	2.912	$0.656 \pm 0.004$	$0.009 \pm 0.001$	$0.430 \pm 0.001$
				0506260401	50.5, 51.5, 39.0				
AWM4	16 04 57.0	+ 23 55 14	0.032	0093060401	15.3, 15.4, 10.9	0.929	$0.511 \pm 0.022$	$0.002 \pm 0.000$	$0.315 \pm 0.002$
CID28	04 54 50.3	−18 06 33	0.034	0140210101	29.0, 28.5, 23.9	0.619	$0.573 \pm 0.027$	$0.009 \pm 0.001$	$0.240 \pm 0.002$
AWM5	16 58 00.8	+ 27 51 16	0.034	0654800201	44.5, 44.1, 37.4	0.708	$0.502 \pm 0.027$	$0.010 \pm 0.001$	$0.282 \pm 0.002$
				0670350701	9.1, 8.9, 6.3				
UGC03957	07 40 59.4	+ 55 25 55	0.034	0653580101	23.5, 24.7, 8.2	1.290	$0.673 \pm 0.019$	$0.008 \pm 0.000$	$0.456 \pm 0.002$
A1314	11 34 50.5	+ 49 03 28	0.034	0149900201	16.1, 16.0, 13.1	0.461	$0.258 \pm 0.029$	$0.025 \pm 0.001$	$0.085 \pm 0.002$
IC1880	03 06 28.7	−09 43 50	0.034	0601930401	56.1, 55.5, 34.0	0.289	$0.354 \pm 0.016$	$0.004 \pm 0.000$	$0.452 \pm 0.004$
2A0335	03 38 40.8	+ 09 58 28	0.035	0147800201	95.1, 96.6, 84.9	3.450	$0.574 \pm 0.003$	$0.007 \pm 0.000$	$0.614 \pm 0.001$
R0340.6−0239	03 40 41.8	−02 39 57	0.035	0741580901	6.3, 7.0, 3.8	0.795	$0.450 \pm 0.034$	$0.009 \pm 0.001$	$0.390 \pm 0.007$
A2052	15 16 44.0	+ 07 01 07	0.035	0109920101	26.7, 27.0, 20.6	2.494	$0.569 \pm 0.007$	$0.002 \pm 0.000$	$0.425 \pm 0.001$
				0401521201	14.9, 15.2, 11.1				
A2147	16 02 18.7	+ 16 01 12	0.035	0505210601	9.4, 9.1, 4.6	2.405	$0.363 \pm 0.036$	$0.014 \pm 0.001$	$0.120 \pm 0.001$
A2063	15 23 05.4	+ 08 36 09	0.035	0200120401	1.3, 6.6, −	2.160	$0.491 \pm 0.014$	$0.004 \pm 0.000$	$0.258 \pm 0.001$
				0550360101	18.9, 21.4, 11.4				

Table E1 – continued

Name	RA	DEC	redshift	ObsID	$t_{\text{exp}}$ [ks]	$M_{500}$ [ $10^{14} M_{\odot}$ ]	$A_{\text{core}}$ [solar]	w	c
S0540	05 40 06.3	−40 50 32	0.036	0149420101	10.7, 11.6, 5.2	1.221	$0.528 \pm 0.031$	$0.005 \pm 0.000$	$0.313 \pm 0.003$
NGC1650	04 45 10.0	−15 51 01	0.036	0741580701	4.9, 5.0, 3.9	0.864	$0.526 \pm 0.078$	$0.019 \pm 0.001$	$0.162 \pm 0.004$
NGC5098	13 20 15.4	+ 33 08 30	0.036	0105860101	29.8, 30.0, 23.3	0.517	$0.341 \pm 0.013$	$0.009 \pm 0.001$	$0.377 \pm 0.003$
A2151	16 04 35.7	+ 17 43 28	0.037	0147210301	7.1, 7.4, 4.5	1.320	$0.352 \pm 0.022$	$0.018 \pm 0.001$	$0.314 \pm 0.003$
R1423.1 + 2615	14 23 10.1	+ 26 15 20	0.037	0670350101	10.0, 10.9, 4.9	0.376	$0.528 \pm 0.040$	$0.020 \pm 0.001$	$0.408 \pm 0.007$
A3570	13 46 52.5	−37 52 28	0.038	0765030701	16.9, 18.0, 11.7	0.699	$0.546 \pm 0.073$	$0.130 \pm 0.007$	$0.050 \pm 0.002$
A0576	07 21 22.2	+ 55 47 11	0.039	0205070301	9.0, 9.7, 6.5	1.681	$0.475 \pm 0.011$	$0.014 \pm 0.001$	$0.206 \pm 0.001$
				0205070401	13.8, 14.5, 10.6				
				0504320201	20.8, 21.7, 14.0				
				0504320101	25.9, 28.4, 16.7				
A1139	10 58 10.4	+ 01 35 11	0.037	0601930101	24.8, 27.5, 17.5	0.439	$0.407 \pm 0.045$	$0.020 \pm 0.001$	$0.087 \pm 0.002$
CID36	05 42 09.3	−26 07 25	0.039	0741581101	10.7, 11.6, 7.9	0.853	$0.362 \pm 0.034$	$0.035 \pm 0.002$	$0.154 \pm 0.003$
A3571	13 47 28.4	−32 50 59	0.039	0086950201	19.7, 19.5, 13.1	4.507	$0.478 \pm 0.014$	$0.011 \pm 0.001$	$0.258 \pm 0.001$
RBS0540	04 25 51.4	−08 33 33	0.040	0300210401	36.0, 35.9, 27.3	2.086	$0.523 \pm 0.010$	$0.003 \pm 0.000$	$0.525 \pm 0.001$
R0748.1 + 1832	07 48 09.5	+ 18 32 47	0.040	0651780201	12.2, 11.9, 7.1	0.520	$0.404 \pm 0.053$	$0.003 \pm 0.000$	$0.159 \pm 0.003$
R0137.2−0912	01 37 15.4	−09 12 10	0.041	0765001101	5.7, 5.6, 3.4	0.947	$0.360 \pm 0.024$	$0.011 \pm 0.001$	$0.367 \pm 0.005$
A2589	23 23 53.5	+ 16 48 32	0.042	0204180101	22.1, 23.1, 17.9	1.990	$0.591 \pm 0.017$	$0.006 \pm 0.000$	$0.284 \pm 0.001$
R1742.8 + 3900	17 42 48.3	+ 39 00 35	0.042	0765040801	12.7, 12.9, 11.2	0.774	$0.208 \pm 0.009$	$0.012 \pm 0.001$	$0.379 \pm 0.004$
A0548	05 45 27.2	−25 56 20	0.042	0302030101	42.7, 42.9, 29.2	0.502	$0.636 \pm 0.060$	$0.012 \pm 0.001$	$0.139 \pm 0.002$
R1740.5 + 3538	17 40 32.7	+ 35 38 51	0.043	0761112101	16.5, 16.1, 12.4	0.914	$0.599 \pm 0.027$	$0.010 \pm 0.001$	$0.344 \pm 0.003$
A0119	00 56 18.3	−01 13 00	0.044	0012440101	22.1, 22.7, 16.2	2.475	$0.338 \pm 0.024$	$0.003 \pm 0.000$	$0.090 \pm 0.001$
				0505211001	9.1, 9.7, 6.3				
A0160	01 13 05.8	+ 15 31 01	0.044	0651780101	11.1, 12.6, 4.9	0.745	$0.462 \pm 0.080$	$0.027 \pm 0.002$	$0.136 \pm 0.003$
S0555	05 57 13.2	−37 27 58	0.044	0765010701	14.7, 14.7, 12.3	0.972	$0.495 \pm 0.024$	$0.003 \pm 0.000$	$0.391 \pm 0.004$
MKW3s	15 21 50.0	+ 07 42 32	0.044	0723801501	100.1, 101.4, 77.9	2.522	$0.529 \pm 0.006$	$0.006 \pm 0.000$	$0.413 \pm 0.001$
A1983	14 52 58.8	+ 16 41 59	0.044	0091140201	23.3, 21.9, 12.5	0.878	$0.525 \pm 0.037$	$0.005 \pm 0.000$	$0.209 \pm 0.002$
RBS0485	03 52 20.7	−54 53 09	0.045	0651580601	22.3, 23.3, 11.4	0.681	$0.539 \pm 0.044$	$0.018 \pm 0.001$	$0.157 \pm 0.003$
A3558C	13 31 32.4	−31 48 55	0.045	0105261401	10.2, 10.5, 6.6	0.833	$0.288 \pm 0.057$	$0.013 \pm 0.001$	$0.114 \pm 0.002$
R1454.4 + 1622	14 54 28.0	+ 16 22 13	0.046	0670350201	15.4, 16.4, 14.9	0.461	$0.243 \pm 0.031$	$0.003 \pm 0.000$	$0.178 \pm 0.004$
A1736	13 26 54.0	−27 11 00	0.046	0505210201	10.1, 9.4, 3.6	2.706	$0.421 \pm 0.044$	$0.042 \pm 0.002$	$0.095 \pm 0.001$
A3376	06 01 45.7	−39 59 34	0.047	0151900101	21.6, 22.0, 15.3	1.976	$0.362 \pm 0.021$	$0.082 \pm 0.005$	$0.109 \pm 0.001$
				0504140101	36.6, 39.0, 28.1				
A1644	12 57 09.7	−17 24 01	0.047	0010420201	12.4, 12.8, 10.0	2.925	$0.464 \pm 0.027$	$0.012 \pm 0.001$	$0.189 \pm 0.001$
A4059	23 57 02.3	−34 45 38	0.048	0723800901	66.9, 68.9, 40.6	2.666	$0.627 \pm 0.006$	$0.004 \pm 0.000$	$0.363 \pm 0.001$
				0723801001	70.6, 70.5, 52.8				
A3558	13 27 57.5	−31 30 09	0.048	0107260101	38.9, 39.4, 32.4	3.974	$0.420 \pm 0.010$	$0.027 \pm 0.002$	$0.200 \pm 0.001$
A3560	13 32 22.6	−33 08 22	0.049	0205450201	26.9, 27.4, 17.5	1.682	$0.396 \pm 0.030$	$0.021 \pm 0.001$	$0.126 \pm 0.001$
A3558B	13 29 42.9	−31 36 09	0.049	0651590201	8.5, 9.7, −	1.721	$0.370 \pm 0.053$	$0.005 \pm 0.000$	$0.173 \pm 0.003$
A2717	00 03 12.1	−35 55 38	0.049	0145020201	46.3, 46.1, 40.2	1.202	$0.588 \pm 0.019$	$0.006 \pm 0.000$	$0.297 \pm 0.001$
A3562	13 33 36.3	−31 39 40	0.049	0105261501	15.6, 17.0, 8.3	2.370	$0.480 \pm 0.015$	$0.008 \pm 0.000$	$0.222 \pm 0.001$
				0105261601	16.2, 15.8, 13.4				
				0105261301	34.9, 35.1, 31.1				
R1022.0 + 3830	10 22 04.7	+ 38 30 43	0.049	0503601301	10.5, 10.1, 7.9	0.701	$0.384 \pm 0.047$	$0.027 \pm 0.002$	$0.325 \pm 0.006$
R2104.9−5149	21 04 54.7	−51 49 35	0.049	0765000101	10.7, 10.6, 6.2	1.323	$0.608 \pm 0.034$	$0.004 \pm 0.000$	$0.414 \pm 0.004$
R1002.6 + 3241	10 02 38.6	+ 32 41 58	0.050	0503600301	8.2, 7.7, 5.7	0.944	$0.348 \pm 0.050$	$0.006 \pm 0.000$	$0.189 \pm 0.005$
R0413.9−3806	04 13 57.1	−38 06 00	0.050	0720251501	8.2, 9.1, 4.0	1.625	$0.553 \pm 0.022$	$0.005 \pm 0.000$	$0.323 \pm 0.003$
				0720253501	11.9, 12.4, 3.5				
A3391	06 26 22.8	−53 41 44	0.051	0505210401	22.2, 21.9, 14.4	2.161	$0.400 \pm 0.022$	$0.011 \pm 0.001$	$0.149 \pm 0.001$
				0720252301	11.0, 11.0, 8.7				
R1337.4−4120	13 37 28.2	−41 20 01	0.052	0765041301	15.7, 16.9, 9.6	0.987	$0.417 \pm 0.045$	$0.008 \pm 0.000$	$0.160 \pm 0.002$
A0151N	01 08 50.1	−15 24 36	0.053	0765001201	6.6, 8.7, −	1.278	$0.513 \pm 0.063$	$0.004 \pm 0.000$	$0.221 \pm 0.004$
A3301	05 00 46.5	−38 40 41	0.054	0083151201	9.7, 9.8, 5.9	1.2705	$0.319 \pm 0.061$	$0.013 \pm 0.001$	$0.161 \pm 0.003$
HYDRA	09 18 06.5	−12 05 36	0.054	0504260101	63.9, 67.6, 44.2	3.624	$0.387 \pm 0.005$	$0.003 \pm 0.000$	$0.494 \pm 0.001$
R0631.3−5610	06 31 20.7	−56 10 20	0.054	0720253401	23.2, 24.3, 19.4	1.286	$0.326 \pm 0.037$	$0.030 \pm 0.002$	$0.127 \pm 0.002$
R0844.9 + 4258	08 44 56.7	+ 42 58 54	0.055	0503600101	15.5, 16.4, 10.9	0.470	$0.447 \pm 0.041$	$0.013 \pm 0.001$	$0.348 \pm 0.006$
A3530	12 55 34.5	−30 19 50	0.054	0201780101	11.0, 10.7, 8.4	1.558	$0.372 \pm 0.046$	$0.011 \pm 0.001$	$0.131 \pm 0.002$
A0754	09 09 08.4	−09 39 58	0.054	0556200101	36.5, 37.4, 21.9	4.482	$0.387 \pm 0.013$	$0.079 \pm 0.004$	$0.143 \pm 0.000$
				0556200501	68.6, 70.7, 49.1				
A3532	12 57 16.9	−30 22 37	0.055	0030140301	7.9, 8.3, 4.6	2.335	$0.412 \pm 0.051$	$0.038 \pm 0.002$	$0.117 \pm 0.002$
A0085	00 41 50.1	−09 18 07	0.055	0723802101	82.2, 85.5, 55.8	5.316	$0.562 \pm 0.004$	$0.009 \pm 0.001$	$0.364 \pm 0.000$
				0723802201	88.7, 91.3, 73.5				
A2319	19 21 08.8	+ 43 57 30	0.056	0302150101	14.6, 14.6, 9.2	5.835	$0.382 \pm 0.008$	$0.025 \pm 0.001$	$0.204 \pm 0.000$
				0302150201	14.3, 14.3, 9.8				

Table E1 – continued

Name	RA	DEC	redshift	ObsID	$t_{\text{exp}}$ [ks]	$M_{500}$ [ $10^{14} M_{\odot}$ ]	$A_{\text{core}}$ [solar]	w	c
				0600040101	46.4, 45.4, 38.9				
R1122.2 + 6712	11 22 14.5	+ 67 12 46	0.056	0503600401	14.9, 14.8, 10.9	0.439	$0.568 \pm 0.063$	$0.008 \pm 0.001$	$0.359 \pm 0.007$
R1256.9–3119	12 56 59.8	−31 19 19	0.056	0765040401	5.7, 6.9, 3.1	1.108	$0.551 \pm 0.133$	$0.005 \pm 0.000$	$0.182 \pm 0.006$
S0868	20 23 01.6	−20 56 55	0.056	0201902301	14.9, 15.4, 7.9	1.182	$0.293 \pm 0.040$	$0.018 \pm 0.001$	$0.197 \pm 0.003$
Sersic	23 13 58.6	−42 44 02	0.058	0147800101	78.8, 78.6, 64.0	2.826	$0.406 \pm 0.005$	$0.005 \pm 0.000$	$0.577 \pm 0.001$
A2626	23 36 30.3	+ 21 08 33	0.055	0083150201	8.7, 8.1, 4.4	1.806	$0.602 \pm 0.013$	$0.006 \pm 0.000$	$0.361 \pm 0.002$
				0148310101	35.5, 36.8, 29.8				
A0133	01 02 42.1	−21 52 25	0.057	0144310101	18.6, 18.8, 13.8	2.477	$0.694 \pm 0.008$	$0.002 \pm 0.000$	$0.402 \pm 0.001$
				0723801301	62.3, 63.5, 49.6				
				0723802001	29.0, 33.2, 14.2				
R1926.9–5342	19 26 58.3	−53 42 11	0.057	0765000601	13.4, 14.9, 7.5	1.489	$0.305 \pm 0.016$	$0.007 \pm 0.000$	$0.468 \pm 0.004$
A2401	21 58 20.1	−20 06 16	0.057	0555220101	50.5, 51.5, 40.3	0.898	$0.338 \pm 0.032$	$0.003 \pm 0.000$	$0.175 \pm 0.002$
R0746.3 + 3100	07 46 37.3	+ 31 00 49	0.058	0503600201	10.4, 10.5, 7.6	0.675	$0.522 \pm 0.073$	$0.009 \pm 0.001$	$0.170 \pm 0.004$
A0152	01 10 05.5	+ 13 58 49	0.058	0503600701	13.2, 13.7, 6.3	0.408	$0.435 \pm 0.083$	$0.009 \pm 0.001$	$0.261 \pm 0.007$
A1991	14 54 31.4	+ 18 38 31	0.059	0145020101	23.5, 24.0, 14.5	1.676	$0.594 \pm 0.016$	$0.002 \pm 0.000$	$0.462 \pm 0.002$
R2124.3–7446	21 24 22.8	−74 46 25	0.059	0765040101	11.5, 12.3, 7.7	1.174	$0.646 \pm 0.050$	$0.006 \pm 0.000$	$0.347 \pm 0.004$
A3266	04 31 24.1	−61 26 38	0.059	0105261101	11.3, 10.8, 6.0	4.558	$0.303 \pm 0.016$	$0.059 \pm 0.003$	$0.133 \pm 0.000$
				0105260701	18.0, 18.3, 12.8				
				0105260901	20.9, 20.9, 14.2				
				0105260801	18.6, 17.8, 12.5				
A3158	03 42 53.9	−53 38 07	0.059	0300210201	17.7, 17.4, 9.1	3.651	$0.431 \pm 0.016$	$0.005 \pm 0.000$	$0.202 \pm 0.001$
				0300211301	7.4, 7.6, 4.0				
S0974	21 47 55.5	−46 00 19	0.059	0765010801	11.1, 12.3, 5.1	1.376	$0.268 \pm 0.028$	$0.020 \pm 0.001$	$0.260 \pm 0.004$
A3651	19 52 16.5	−55 03 42	0.060	0720252001	3.9, 3.8, 2.4	1.475	$0.383 \pm 0.045$	$0.015 \pm 0.001$	$0.111 \pm 0.002$
S0384	03 45 45.7	−41 12 27	0.060	0201900801	11.0, 12.5, 2.1	1.270	$0.632 \pm 0.025$	$0.006 \pm 0.000$	$0.418 \pm 0.004$
				0404910301	12.9, 13.6, 6.1				
R0225.1–2928	02 25 10.5	−29 28 26	0.060	0302610601	14.7, 15.2, 7.2	1.121	$0.678 \pm 0.055$	$0.017 \pm 0.001$	$0.259 \pm 0.004$
S0405	03 51 08.9	−82 13 00	0.061	0675471101	6.4, 7.4, 1.9	2.192	$0.317 \pm 0.034$	$0.016 \pm 0.001$	$0.163 \pm 0.002$
				0720250601	3.7, 10.3, 6.1				
A2622	23 35 05.0	+ 27 22 12	0.061	0765020701	19.2, 18.9, 14.1	1.336	$0.577 \pm 0.038$	$0.004 \pm 0.000$	$0.373 \pm 0.004$
A2734	00 11 20.7	−28 51 18	0.062	0675470801	9.4, 10.1, 6.3	2.061	$0.419 \pm 0.042$	$0.016 \pm 0.001$	$0.204 \pm 0.002$
A0602	07 53 24.2	+ 29 21 58	0.062	0761112401	9.2, 9.3, 7.0	1.424	$0.397 \pm 0.048$	$0.048 \pm 0.003$	$0.122 \pm 0.002$
A1795	13 48 53.0	+ 26 35 44	0.062	0097820101	34.3, 32.5, 23.3	5.528	$0.471 \pm 0.008$	$0.006 \pm 0.000$	$0.471 \pm 0.001$
S0239	02 16 42.3	−47 49 24	0.064	0501110201	38.3, 38.2, 27.7	1.008	$0.479 \pm 0.034$	$0.003 \pm 0.000$	$0.214 \pm 0.003$
A3122	03 22 18.6	−41 21 34	0.064	0720253201	21.4, 22.1, 17.1	1.424	$0.325 \pm 0.044$	$0.045 \pm 0.003$	$0.115 \pm 0.002$
S1136	23 36 17.0	−31 36 37	0.064	0765041001	9.8, 10.2, 6.8	1.289	$0.560 \pm 0.073$	$0.004 \pm 0.000$	$0.153 \pm 0.003$
R2306.8–1324	23 06 51.7	−13 24 59	0.066	0765030201	7.9, 9.0, 5.5	1.085	$0.330 \pm 0.065$	$0.028 \pm 0.002$	$0.345 \pm 0.008$
S0112	00 57 48.1	−66 48 44	0.067	0653880201	31.2, 33.4, 20.4	1.620	$0.360 \pm 0.039$	$0.062 \pm 0.003$	$0.152 \pm 0.002$
A0500	04 38 54.7	−22 06 49	0.067	0720253301	29.7, 28.7, 24.9	1.509	$0.510 \pm 0.037$	$0.008 \pm 0.001$	$0.142 \pm 0.002$
A3497	12 00 05.0	−31 24 21	0.069	0761112801	7.2, 7.6, 4.8	1.565	$0.352 \pm 0.046$	$0.042 \pm 0.002$	$0.212 \pm 0.004$
S0987	22 01 50.9	−22 26 40	0.069	0765030901	13.7, 13.7, 10.8	1.457	$0.212 \pm 0.046$	$0.005 \pm 0.000$	$0.208 \pm 0.004$
A3490	11 45 19.1	−34 25 43	0.070	0720252801	12.3, 11.0, 10.0	1.640	$0.420 \pm 0.046$	$0.007 \pm 0.000$	$0.154 \pm 0.002$
A1837	14 01 36.7	−11 07 28	0.070	0109910101	43.7, 43.5, 35.8	1.482	$0.517 \pm 0.024$	$0.013 \pm 0.001$	$0.194 \pm 0.001$
Z1420 + 4933	14 21 35.5	+ 49 33 07	0.072	0765020201	8.8, 8.3, 6.8	1.687	$0.422 \pm 0.031$	$0.011 \pm 0.001$	$0.358 \pm 0.004$
A3104	03 14 19.8	−45 25 27	0.072	0765000401	12.7, 12.6, 10.1	1.979	$0.632 \pm 0.031$	$0.009 \pm 0.001$	$0.370 \pm 0.003$
A0399	02 57 49.8	+ 13 02 57	0.072	0112260101	10.6, 10.8, 5.4	4.245	$0.253 \pm 0.030$	$0.046 \pm 0.003$	$0.164 \pm 0.002$
A2065	15 22 26.5	+ 27 42 34	0.072	0112240201	9.9, 9.2, 6.2	3.508	$0.388 \pm 0.018$	$0.033 \pm 0.002$	$0.234 \pm 0.001$
				0202080201	18.4, 18.2, 12.9				
A1775	13 41 53.8	+ 26 22 19	0.072	0108460101	21.0, 20.9, 16.2	2.478	$0.608 \pm 0.028$	$0.007 \pm 0.000$	$0.412 \pm 0.002$
S0810	19 12 40.3	−75 17 30	0.073	0720251001	15.3, 15.0, 12.1	2.154	$0.467 \pm 0.030$	$0.020 \pm 0.001$	$0.309 \pm 0.003$
R1539.5–8335	15 39 33.9	−83 35 32	0.073	0720252501	10.1, 10.4, 8.1	3.177	$0.625 \pm 0.025$	$0.002 \pm 0.000$	$0.606 \pm 0.004$
A1589	12 41 19.1	+ 18 34 16	0.073	0149900301	14.0, 13.6, 11.1	1.793	$0.391 \pm 0.047$	$0.023 \pm 0.001$	$0.105 \pm 0.002$
S0792	17 05 10.3	−82 10 26	0.074	0761111801	10.7, 11.3, 8.2	1.815	$0.390 \pm 0.044$	$0.004 \pm 0.000$	$0.280 \pm 0.004$
A0401	02 58 57.5	+ 13 34 46	0.074	0112260301	12.2, 11.6, 7.4	5.849	$0.405 \pm 0.028$	$0.010 \pm 0.001$	$0.208 \pm 0.001$
Z4905 + 0523	12 10 18.8	+ 05 23 06	0.075	0765030501	7.3, 7.1, 4.9	1.616	$0.559 \pm 0.082$	$0.010 \pm 0.001$	$0.227 \pm 0.004$
A3825	21 58 27.2	−60 23 58	0.075	0675472201	12.4, 12.4, 10.0	2.002	$0.357 \pm 0.071$	$0.009 \pm 0.001$	$0.078 \pm 0.002$
A3112	03 17 58.5	−44 14 20	0.075	0603050101	80.6, 83.3, 52.6	4.395	$0.660 \pm 0.006$	$0.011 \pm 0.001$	$0.505 \pm 0.001$
				0603050201	66.1, 66.3, 44.9				
A3806	21 46 20.9	−57 17 19	0.076	0675472101	12.6, 12.2, 10.2	1.841	$0.409 \pm 0.036$	$0.011 \pm 0.001$	$0.276 \pm 0.003$
A3822	21 54 09.2	−57 51 19	0.076	0675470401	9.5, 10.7, 2.9	3.050	$0.352 \pm 0.031$	$0.018 \pm 0.001$	$0.146 \pm 0.002$
				0720250301	8.0, 8.1, 3.4				
A2670	23 54 13.4	−10 24 46	0.076	0108460301	12.2, 12.4, 6.9	2.316	$0.527 \pm 0.040$	$0.008 \pm 0.000$	$0.235 \pm 0.003$
Z1215 + 0349	12 17 40.6	+ 03 39 45	0.077	0300211401	21.8, 22.1, 13.9	3.592	$0.331 \pm 0.024$	$0.009 \pm 0.001$	$0.158 \pm 0.001$



Table E1 – *continued*

Name	RA	DEC	redshift	ObsID	$t_{\text{exp}}$ [ks]	$M_{500}$ [ $10^{14} M_{\odot}$ ]	$A_{\text{core}}$ [solar]	w	c
A2029	15 10 55.0	+ 05 43 12	0.077	0111270201	10.6, 11.0, 8.2	7.271	$0.574 \pm 0.010$	$0.003 \pm 0.000$	$0.465 \pm 0.001$
				0551780201	28.7, 31.3, 15.0				
				0551780301	35.5, 36.7, 21.4				
				0551780401	29.2, 30.4, 14.3				
				0551780501	22.8, 23.2, 16.2				
A1648	12 58 49.8	−26 40 03	0.077	0765040701	11.4, 11.7, 9.0	1.601	$0.184 \pm 0.050$	$0.015 \pm 0.001$	$0.127 \pm 0.004$
A3638	19 25 29.6	−42 56 57	0.077	0765020101	11.2, 11.7, 7.5	1.859	$0.475 \pm 0.030$	$0.005 \pm 0.000$	$0.395 \pm 0.004$
A2061	15 21 17.0	+ 30 38 24	0.078	0721740101	44.0, 43.4, 35.7	2.854	$0.255 \pm 0.020$	$0.050 \pm 0.003$	$0.084 \pm 0.001$
A1205	11 13 20.7	+ 02 31 56	0.078	0720250701	7.0, 7.2, 4.8	2.043	$0.555 \pm 0.112$	$0.059 \pm 0.003$	$0.106 \pm 0.003$
R2344.2–0422	23 44 16.0	−04 22 03	0.079	0677180501	11.6, 11.6, 6.9	2.822	$0.431 \pm 0.035$	$0.010 \pm 0.001$	$0.199 \pm 0.002$
A1035	10 32 14.8	+ 40 15 53	0.079	0653810501	15.1, 15.2, 12.6	1.712	$0.515 \pm 0.050$	$0.009 \pm 0.001$	$0.336 \pm 0.005$
R2224.5–5515	22 24 27.5	−55 15 22	0.079	0765020801	10.8, 11.0, 6.0	1.772	$0.387 \pm 0.080$	$0.028 \pm 0.002$	$0.112 \pm 0.003$
R0229.3–3332	02 29 22.3	−33 32 16	0.079	0677180801	6.8, 7.4, 3.9	1.362	$0.280 \pm 0.063$	$0.011 \pm 0.001$	$0.382 \pm 0.006$
S0700	12 36 44.7	−33 54 10	0.080	0201903701	11.6, 11.9, 7.4	1.633	$0.523 \pm 0.026$	$0.011 \pm 0.001$	$0.280 \pm 0.003$
				0302610701	21.9, 22.0, 15.9				
A3771	21 29 51.0	−50 48 04	0.080	0201902501	16.5, 17.7, 8.9	1.614	$0.418 \pm 0.041$	$0.042 \pm 0.002$	$0.102 \pm 0.002$
				0654440201	24.9, 31.7, 8.3				
A2377	21 45 54.8	−10 06 16	0.081	0675472001	10.8, 11.3, 4.8	2.034	$0.539 \pm 0.058$	$0.007 \pm 0.000$	$0.160 \pm 0.003$
A2255	17 12 47.2	+ 64 03 41	0.081	0112260801	7.6, 7.4, 2.9	3.741	$0.362 \pm 0.062$	$0.104 \pm 0.006$	$0.121 \pm 0.006$
A2402	21 58 30.5	−09 48 28	0.081	0765030101	9.1, 9.0, 5.4	1.787	$0.623 \pm 0.055$	$0.008 \pm 0.000$	$0.426 \pm 0.006$
A2410	22 02 05.9	−09 49 28	0.081	0720252101	12.5, 12.4, 7.6	1.788	$0.386 \pm 0.069$	$0.015 \pm 0.001$	$0.172 \pm 0.004$
A0653	08 21 51.7	+ 01 12 42	0.082	0201903601	10.3, 9.8, 6.2	1.479	$0.345 \pm 0.047$	$0.020 \pm 0.001$	$0.198 \pm 0.004$
				0404911201	13.7, 14.0, 8.8				
A2566	23 16 07.5	−20 27 19	0.082	0677180301	7.1, 8.4, 3.6	2.173	$0.577 \pm 0.027$	$0.003 \pm 0.000$	$0.476 \pm 0.004$
R2143.9–5637	21 43 58.3	−56 37 35	0.082	0675471901	12.5, 12.4, 10.2	2.650	$0.443 \pm 0.025$	$0.005 \pm 0.000$	$0.477 \pm 0.004$
A2428	22 16 15.5	−09 20 24	0.083	0675472401	10.4, 10.0, 7.9	2.412	$0.467 \pm 0.031$	$0.008 \pm 0.000$	$0.337 \pm 0.003$
A2245	17 02 31.9	+ 33 30 47	0.084	0672910101	12.4, 13.0, 10.0	1.242	$0.604 \pm 0.070$	$0.013 \pm 0.001$	$0.210 \pm 0.005$
A1650	12 58 41.1	−01 45 25	0.084	0093200101	32.2, 32.5, 26.9	4.121	$0.456 \pm 0.016$	$0.007 \pm 0.000$	$0.323 \pm 0.001$
A1651	12 59 21.5	−04 11 41	0.085	0203020101	7.7, 8.2, 5.8	4.393	$0.517 \pm 0.025$	$0.008 \pm 0.000$	$0.290 \pm 0.002$
A2420	22 10 19.7	−12 10 34	0.085	0675470501	11.9, 12.5, 9.0	3.514	$0.481 \pm 0.036$	$0.027 \pm 0.002$	$0.159 \pm 0.002$
A1663	13 02 50.7	−02 30 22	0.085	0201901801	21.7, 21.6, 15.0	1.605	$0.703 \pm 0.040$	$0.030 \pm 0.002$	$0.310 \pm 0.003$
A1750	13 30 49.9	−01 52 22	0.085	0112240301	25.9, 27.1, 20.8	3.057	$0.412 \pm 0.039$	$0.018 \pm 0.001$	$0.186 \pm 0.002$
A2597	23 25 20.0	−12 07 38	0.085	0723801601	20.6, 22.4, 9.2	4.182	$0.413 \pm 0.007$	$0.003 \pm 0.000$	$0.580 \pm 0.002$
				0723801701	41.3, 45.2, 20.2				
A3126	03 28 37.5	−55 42 46	0.085	0675471001	5.1, 5.2, 3.0	2.437	$0.539 \pm 0.054$	$0.004 \pm 0.000$	$0.218 \pm 0.004$
				0720250501	5.0, 6.0, −				
A2556	23 13 00.9	−21 37 55	0.087	0677180201	8.4, 8.5, 4.2	2.476	$0.510 \pm 0.036$	$0.007 \pm 0.000$	$0.460 \pm 0.004$
R1309.2–0136	13 09 17.0	−01 36 45	0.088	0201750201	6.1, 6.0, 5.0	1.860	$0.756 \pm 0.103$	$0.010 \pm 0.001$	$0.294 \pm 0.006$
A0478	04 13 25.6	+ 10 28 01	0.088	0109880101	62.1, 67.0, 44.1	6.424	$0.458 \pm 0.007$	$0.003 \pm 0.000$	$0.455 \pm 0.001$
A0278	01 57 25.7	+ 32 13 26	0.089	0203980101	20.4, 21.0, 15.7	1.480	$0.265 \pm 0.039$	$0.012 \pm 0.001$	$0.219 \pm 0.003$
A2142	15 58 20.6	+ 27 13 37	0.091	0674560201	48.7, 48.5, 37.5	8.149	$0.408 \pm 0.010$	$0.009 \pm 0.001$	$0.323 \pm 0.001$
A3695	20 34 47.9	−35 48 48	0.089	0675470301	10.4, 10.6, 7.6	3.730	$0.387 \pm 0.045$	$0.019 \pm 0.001$	$0.127 \pm 0.002$
A3998	23 21 33.4	−41 53 56	0.089	0677180401	7.4, 8.2, 4.3	2.586	$0.591 \pm 0.041$	$0.005 \pm 0.000$	$0.391 \pm 0.004$
A2442	22 25 51.0	−06 36 12	0.090	0677182201	7.6, 8.5, 3.2	1.912	$0.378 \pm 0.044$	$0.006 \pm 0.000$	$0.251 \pm 0.005$
				0677182701	7.7, 8.0, 5.7				
R1301.6–0650	13 01 36.3	−06 50 00	0.090	0677181701	11.4, 10.8, 8.1	1.588	$0.519 \pm 0.078$	$0.022 \pm 0.001$	$0.344 \pm 0.008$
UGC09480	14 42 18.4	+ 22 18 17	0.090	0765010501	11.0, 10.8, 6.4	2.323	$0.582 \pm 0.040$	$0.003 \pm 0.000$	$0.448 \pm 0.005$
Z1703–0132	17 06 26.6	−01 32 23	0.091	0675471401	6.2, 6.4, 4.3	2.139	$0.470 \pm 0.059$	$0.017 \pm 0.001$	$0.128 \pm 0.003$
				0720250901	7.7, 7.1, 5.7				
A3358	05 38 16.3	−20 37 23	0.091	0677181201	8.7, 8.7, 7.7	1.887	$0.335 \pm 0.057$	$0.012 \pm 0.001$	$0.157 \pm 0.003$
A0761	09 10 36.3	−10 34 52	0.092	0765040601	6.4, 6.7, 3.1	1.994	$0.405 \pm 0.087$	$0.007 \pm 0.000$	$0.167 \pm 0.004$
A2700	00 03 50.6	+ 02 03 48	0.092	0201900101	23.1, 23.4, 15.3	1.734	$0.447 \pm 0.039$	$0.003 \pm 0.000$	$0.245 \pm 0.003$
R0548.8–2154	05 48 50.4	−21 54 43	0.093	0677181301	22.5, 23.0, 18.6	1.659	$0.442 \pm 0.048$	$0.048 \pm 0.003$	$0.095 \pm 0.002$
A2312	18 53 58.1	+ 68 22 53	0.093	0692930701	13.8, 13.7, 6.8	2.041	$0.539 \pm 0.059$	$0.042 \pm 0.002$	$0.230 \pm 0.003$
A3694	20 34 42.1	−34 04 26	0.094	0675471701	10.4, 10.8, 8.1	2.744	$0.521 \pm 0.040$	$0.023 \pm 0.001$	$0.289 \pm 0.003$
A0013	00 13 38.3	−19 30 08	0.094	0200270101	29.5, 29.5, 25.4	2.182	$0.357 \pm 0.037$	$0.023 \pm 0.001$	$0.163 \pm 0.002$
A3921	22 49 57.0	−64 25 46	0.094	0112240101	27.6, 26.6, −	3.614	$0.372 \pm 0.022$	$0.010 \pm 0.001$	$0.192 \pm 0.001$
RBS1847	22 18 05.5	−65 11 06	0.095	0675470701	11.9, 12.6, 9.2	2.795	$0.400 \pm 0.037$	$0.011 \pm 0.001$	$0.272 \pm 0.003$
A2244	17 02 42.9	+ 34 03 43	0.095	0740900101	24.1, 24.1, 18.1	4.491	$0.425 \pm 0.018$	$0.007 \pm 0.000$	$0.349 \pm 0.001$
A4010	23 31 12.7	−36 30 24	0.096	0404520501	17.1, 16.7, 12.3	3.282	$0.723 \pm 0.034$	$0.006 \pm 0.000$	$0.411 \pm 0.003$
A3911	22 46 18.6	−52 43 46	0.097	0149670301	22.1, 22.4, 16.5	3.399	$0.331 \pm 0.031$	$0.008 \pm 0.001$	$0.110 \pm 0.001$
R1558.3–1410	15 58 23.2	−14 10 04	0.097	0675472901	9.6, 10.5, 7.5	3.873	$0.561 \pm 0.015$	$0.005 \pm 0.000$	$0.425 \pm 0.002$
				0720253101	29.0, 29.8, 21.8				

Table E1 – continued

Name	RA	DEC	redshift	ObsID	$t_{\text{exp}}$ [ks]	$M_{500}$ [ $10^{14} M_{\odot}$ ]	$A_{\text{core}}$ [solar]	$w$	$c$
A2175	16 20 31.7	+ 29 53 43	0.097	0692930901	10.4, 10.1, 8.4	2.573	$0.440 \pm 0.057$	$0.009 \pm 0.001$	$0.176 \pm 0.003$
R1931.6–3354	19 31 38.7	−33 54 47	0.097	0675471601	9.9, 9.7, 6.5	2.381	$0.451 \pm 0.039$	$0.003 \pm 0.000$	$0.421 \pm 0.005$
R1633.8–0738	16 33 53.9	−07 38 42	0.097	0677181901	10.7, 11.3, 6.1	1.614	$0.206 \pm 0.082$	$0.029 \pm 0.002$	$0.130 \pm 0.004$
A3827	22 01 56.0	−59 56 58	0.098	0149670101	19.3, 19.1, 14.6	4.589	$0.403 \pm 0.025$	$0.004 \pm 0.000$	$0.233 \pm 0.001$
A2426	22 14 32.6	−10 22 18	0.098	0675470601	10.1, 10.1, 7.8	3.558	$0.592 \pm 0.036$	$0.007 \pm 0.000$	$0.313 \pm 0.003$
A0550	05 52 52.4	−21 03 25	0.099	0675470101	5.1, 6.6, –	3.191	$0.442 \pm 0.032$	$0.025 \pm 0.001$	$0.175 \pm 0.002$
A4067	23 59 19.2	−60 42 00	0.099	0720250101	15.2, 15.0, 12.7				
				0677180601	9.9, 10.1, 8.0	1.970	$0.635 \pm 0.089$	$0.099 \pm 0.005$	$0.147 \pm 0.003$

This paper has been typeset from a  $\text{\LaTeX}$  file prepared by the author.